Titre: Title:	Investigation of differential diffusion in lean, premixed, hydrogen-enriched swirl flames
Auteurs: Authors:	Benjamin Francolini, Luming Fan, Ehsan Abbasi-Atibeh, Gilles Bourque, Patrizio Vena, & Jeffrey M. Bergthorson
Date:	2024
Type:	Article de revue / Article
Référence: Citation:	Francolini, B., Fan, L., Abbasi-Atibeh, E., Bourque, G., Vena, P., & Bergthorson, J. M. (2024). Investigation of differential diffusion in lean, premixed, hydrogen-enriched swirl flames. Applications in Energy and Combustion Science, 18, 100272 (16 pages). https://doi.org/10.1016/j.jaecs.2024.100272

URL de PolyPublie: PolyPublie URL:	https://publications.polymtl.ca/58564/
Version:	Version officielle de l'éditeur / Published version Révisé par les pairs / Refereed
Conditions d'utilisation: Terms of Use:	CC BY-NC-ND

Titre de la revue: Journal Title:	Applications in Energy and Combustion Science (vol. 18)
Maison d'édition: Publisher:	Elsevier
URL officiel: Official URL:	https://doi.org/10.1016/j.jaecs.2024.100272
Mention légale: Legal notice:	© 2024 The Authors. Published by Elsevier Ltd. This is an open access article under the CC BY-NC-ND license (http://creativecommons.org/licenses/bync-nd/4.0/).

Check for updates

Investigation of differential diffusion in lean, premixed, hydrogen-enriched swirl flames

Benjamin Francolini [a,*], Luming Fan [b], Ehsan Abbasi-Atibeh [a], Gilles Bourque [a,c], Patrizio Vena [b,d], Jeffrey Bergthorson [a]

[a] Department of Mechanical Engineering, McGill University, 845 Sherbrooke Street West, Montréal, H3A 0G4, Québec, Canada
[b] Gas Turbine Laboratory, Aerospace Research Centre, National Research Council Canada, 1200 Montreal Rd, Ottawa, K1A 0R6, Ontario, Canada
[c] Siemens Canada Limited, 9505 Chemin de la Côte de Liesse, Montréal, H9P 1A5, Québec, Canada
[d] Department of Mechanical Engineering, Polytechnique Montréal, 2500 chemin de Polytechnique, Montréal, H3T 1J4, Québec, Canada

A B S T R A C T

Hydrogen combustion is a promising alternative to fossil fuel combustion in an effort to reduce our carbon footprint. However, hydrogen combustion is prone to thermodiffusive instabilities largely dependent on differential diffusion, a phenomenon that can lead to higher probabilities of flashback in industrial burners, given hydrogen's high reactivity and diffusivity. This paper evaluates low-swirl flames of methane and air enriched with hydrogen to highlight the onset of differential diffusion. Testing was conducted in a fully controllable swirl burner, where bulk velocity U_{av} = 13 m/s and swirl number S = 0.6 were kept constant for each hydrogen–methane blend to isolate increases in flame surface area from increases in turbulence intensity. Furthermore, each fuel blend of hydrogen and methane is evaluated at the same laminar flame speed of S_L^o = 0.267 m/s to isolate flame stretch effects on the turbulent burning rate. Combined hydroxyl (OH) PLIF and stereoscopic PIV at the National Research Council of Canada were used to analyze the OH fluorescence in a 2D-3C velocity field for each flame condition. High-speed PIV at McGill University was used to resolve local flame phenomena, such as local flame displacement velocity and flame stretch rate. Using these techniques, it can be observed that the flame displaces axially in response to turbulent flame speed while exhibiting increases in flamefront wrinkling. This increased corrugation due to flame stretch is highlighted in the PDFs of local curvature and κS_f and is further evidenced by a shift towards positive curvatures ($\kappa > 0$) for increasing H_2 volume fraction. This trend suggests that there is a strong correlation with increases in turbulent burning rate and positive curvature as a result of differential diffusion, but it is not necessarily a control mechanism of the most forward propagating points proposed by *the theory of leading points*.

1. Introduction

The climate crisis remains the most significant problem today, largely due to increasing greenhouse gas (GHG) emissions from fossil fuel combustion. In an effort to mitigate global warming from GHGs, the Intergovernmental Panel on Climate Change (IPCC) projects a required annual decrease of ≈8% of CO_2 emissions (until the year 2100) to limit anthropogenic warming to 1.5 °C above pre-industrial levels [1]. However, as of 2018, our global energy framework is 85.5% dependent on fossil fuels (i.e., coal, oil, natural gas), with natural gas set to contribute a larger percentage of the fossil fuel energy mix during the 2020s [2]. Therefore, it is imperative to employ greener energy alternatives in order to meet increasingly stringent emissions targets while also rapidly transitioning away from carbon-based fuels.

Hydrogen is a desirable fuel gaining traction because its combustion produces zero carbon emissions and its utilization can be quickly realizable in many practical combustion applications. Currently, hydrogen fuel is conventionally produced through steam methane reforming (i.e., "grey hydrogen"), which is a carbon-intensive process [3]. Alternatively, hydrogen production can become greener through natural gas pyrolysis (i.e., "turquoise hydrogen"), water electrolysis (i.e., "green hydrogen"), and new approaches such as metal-water reactions [4,5], as significant international investment looks to ensure its feasibility and scalability [6,7]. Hydrogen is therefore generating significant interest as a fuel of the future, in particular for gas turbines in the power generation sector, where major engine manufacturers are prioritizing

Nomenclature	
α	Thermal diffusivity
κ	Local curvature
Λ	Integral length scale
$\mathcal{D}$	Mass diffusivity of deficient reactant
ϕ	Equivalence ratio
Σ	Flame surface density
A_{L}	Laminar flame surface area
A_{T}	Turbulent flame surface area
c	Progress variable
I_{o}	Stretch factor
K	Flame stretch rate
$K_{\mathrm{s,t}}$	Local hydrodynamic strain rate
l_{K}	Kolmogorov length scale
S	Geometric swirl number
$S_{\mathrm{L}}^{\mathrm{o}}$	Unstretched laminar flame speed
S_{C}	Turbulent flame speed as consumption speed
S_{flame}	Velocity of flamefront in lab reference
S_{f}	Turbulent flame speed as local flame displacement velocity
S_{L}	Stretched laminar flame speed
S_{T}	Turbulent flame speed
S_{u}	Convective flow velocity upstream of flame
U_{av}	Bulk velocity
X	Mole fraction
FOV	Field of view
FSA	Flame surface area
$\mathrm{Le}_{\mathrm{eff}}$	Effective Lewis number
PDF	Probability density function
PIV	Particle image velocimetry
PLIF	Planar laser-induced fluorescence

Fig. 1. Representation of Damköhler's first hypothesis on the proportionality of the normalized flame speed and normalized FSA.

combustion with Le < 1, the mixture is termed thermodiffusively unstable. The mechanism behind such unstable flames, particularly for fuel-lean hydrogen combustion, occurs primarily through hydrogen's preferential diffusion towards the positively curved regions of the flamefront. As a result, such regions will have a higher local stoichiometry (i.e., local ϕ) than regions of negative curvature [14], which results in higher local temperatures. Since the temperature is higher in the positively-curved regions, the local burning rate increases, and these regions will propagate faster. This consequence of hydrogen's enhanced diffusion is the basis of the *theory of leading points* proposed by Kuznetsov [19], which suggests that the turbulent burning rate is effectively controlled by the displacement speed of the most positively-curved regions of the flamefront (i.e., "leading points"). This contrasts Damköhler's first hypothesis stating that the turbulent burning rate is largely a product of flamefront wrinkling such that the turbulent flame speed is proportional to the turbulent flame surface area, as shown in Fig. 1 (i.e. $S_{\mathrm{T}}A_{\mathrm{L}} \sim S_{\mathrm{L}}\,A_{\mathrm{T}}$).

However, Venkateswaran et al. [20] have demonstrated that the increasing critical stretch rate in high-hydrogen content mixtures plays a significant role in increasing the stretched laminar flame speed S_{L} and by consequence, the burning rate. Damköhler's theory on the turbulent burning rate has since been modified, but consensus remains to be reached on a universal definition for the turbulent flame speed [21]. One such definition of the turbulent flame speed S_{T} incorporates flame stretch sensitivity as a stretch factor I_{o} [22,23]:

$$S_{\mathrm{T}} = I_{\mathrm{o}} S_{\mathrm{L}}^{\mathrm{o}} \int_{-\infty}^{\infty} \Sigma \, d\eta \qquad (2)$$

This formulation depends on three parameters: (1) the unstretched laminar flame speed $S_{\mathrm{L}}^{\mathrm{o}}$, (2) the flame surface area (FSA) ratio $A_{\mathrm{T}}/A_{\mathrm{L}}$, which can be thought of as proportional to the maximum flame surface density Σ (calculated at $\bar{c} = 0.5$) multiplied by the turbulent flame brush δ_{T} and (3) the stretch factor I_{o}, which is largely influenced by differential diffusion. For reference, Bray and Cant [24] define the stretch factor I_{o} as the averaged normalized consumption speed $S_{\mathrm{C}}/S_{\mathrm{L}}$. For thermodiffusively-stable flames (Le ≥ 1), combustion models assume an $I_{\mathrm{o}} \approx 1$, which renders Eq. (2) to be consistent with Damköhler's hypothesis [25]. However, in thermodiffusively-unstable hydrogen flames with Le < 1, stretch significantly impacts local flame dynamics, resulting in a tendency for I_{o} to be larger. Several studies highlight the influence of I_{o} on the turbulent burning rate [26,27], but further understanding is required on the direct effect of hydrogen enrichment on the stretch factor. This problem is largely due the tendency for I_{o} to become strongly coupled to FSA generation, since increases in the turbulent flame speed, particularly in thermodiffusively unstable mixtures, stretch the flame further upstream and ultimately enhance FSA [20]. Abbasi-Atibeh et al. [15,16] attempted to determine if a correlation existed between the stretched flame speed and FSA generation for various Lewis number mixtures, primarily by keeping

fuel flexibility with hydrogen enriched natural gas as they gradually transition to 100% hydrogen.

The inherent high reactivity and molecular diffusivity of hydrogen [8,9] make the behavior of H_2-enriched flames difficult to reliably predict. A better understanding is thus crucial to mitigate potential issues such as flashback, acoustic instability, and emissions of NO_x [10,11], which are key considerations in the integration of hydrogen into gas turbine burners/combustors. Consequently, this has become an active area of research, where hydrogen enrichment has been reported to increase the laminar flame speed (S_{L}) and adiabatic flame temperature [12] while decreasing the lean stability limit [13]. The influence of hydrogen enrichment on flame topology has been well-documented in Bunsen [14], counter-flow [15,16], and swirl-stabilized [17] flames and can be characterized by the non-dimensional Lewis number,

$$\mathrm{Le} = \frac{\alpha}{\mathcal{D}} \qquad (1)$$

where, α is the thermal diffusivity of the mixture ($\alpha = \lambda/\rho c_p$), and $\mathcal{D}$ is the molecular diffusivity of the deficient reactant (i.e., fuel for fuel-lean mixtures, oxidizer for fuel-rich mixtures). The Lewis number for methane is close to unity but, as hydrogen content is increased in a fuel-lean, methane–hydrogen–air mixture, the mass diffusivity of the fuel-blend becomes larger than the thermal diffusivity of the mixture, and the Lewis number decreases [18]. This is a result of hydrogen's high molecular diffusivity, namely because it is a smaller and lighter molecule than methane diffusing in the same bulk gas (i.e., air). This leads to *differential diffusion* [16] where, for fuel-lean hydrogen–air
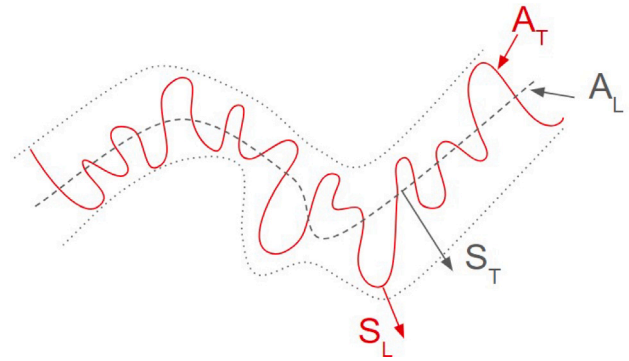
bulk flow properties and unstretched laminar flame speed constant. In their study, they estimated stretch sensitivity to be the ratio between local flame displacement speed S_f and laminar flame speed S_L. In the present work, the turbulent flame speed as S_f evaluated at isosurface A_T is defined as follows:

$$S_f = (S_u + S_{flame}) \cdot \mathbf{n} \tag{3}$$

In this formulation, both S_u and S_{flame} velocity components are considered normal $\mathbf{n}$ to the flame, where S_u is the convective velocity of the gas and S_{flame} is the velocity of the flamefront in the lab reference. In the present study, a similar approach to Abbasi-Atibeh et al. in keeping flow and flame properties constant is used to characterize differential diffusion and the mechanisms responsible for enhancing the turbulent burning rate in a low-swirl flame configuration closer to those present in existing gas turbines. Contrary to high-swirl flames stabilizing through an induced central recirculation zone, low-swirl flames stabilize wherever the local axial flow velocity equals the local flame velocity, often leading to lifted, stable flames [28]. This momentum balance can be described by the following equation [29]:

$$1 - \frac{d\overline{U}}{dz}\frac{(z_f - z_o)}{\overline{U}} = \frac{S_T}{\overline{U}} = \frac{S_L + \mathcal{K}u'}{\overline{U}} \tag{4}$$

Here, $d\overline{U}/dz/\overline{U}$ is the normalized axial divergence rate analogous to the axial stretch rate of the velocity profile upstream of the flame, z_f and z_o are the flame brush position and its virtual origin respectively, S_T is the turbulent flame speed, $\overline{U}$ is the bulk velocity, u' is the RMS velocity and $\mathcal{K}$ is an empirical constant linked to flame stretch. This empirical constant is fundamentally different from the flame stretch rate, K:

$$K = \kappa S_f + K_{s,t} \tag{5}$$

Here, flame stretch is a function of the local flame curvature κ, the local hydrodynamic strain $K_{s,t}$ and the turbulent flame speed as a local flame displacement speed S_f, which is prone to enhance with differential diffusion. It is important to note that Eq. (4) considers these flame parameters on an average basis to demonstrate the global stabilization of the low-swirl flame and to demonstrate the linear dependence of flame stretch on the turbulent flame speed. Conversely, Eq. (5) considers instantaneous flame parameters such as the stretched flame speed S_f, curvature κ and hydrodynamic strain K_{s-t}. Therefore, through complementary experiments employing simultaneous OH-PLIF/stereo-PIV and high-speed PIV, this study aims to provide a greater understanding of differential diffusion effects in hydrogen-enriched flames. Utilizing a newly designed dual-plenum low-swirl burner, the unstretched laminar flame speed S_L^o and the turbulent flowfield are held constant for lean methane/hydrogen–air flames with a varying fuel composition from 100% methane to 20% methane and 80% hydrogen by volume. We thus isolate the specific effect of Lewis number on the turbulent flame structure, the turbulent flame surface area A_T, the flame stretch K, and the turbulent flame speed, S_f, for Le ranging from 0.99 to 0.45. Overall, the results and analyses presented in this study on flame behavior at low Lewis numbers will provide validation in modeling differential diffusion effects in hydrogen-enriched mixtures. More importantly, this study serves as an important step towards designing fuel-flexible combustors cable of integrating and utilizing hydrogen as a means of ensuring environmental sustainability.

2. Experimental methods

2.1. Burner apparatus

A fully-controllable swirl burner was designed and tested at McGill University to study lifted, unconfined swirling flames. The burner is comprised of a feeding block with four tangential inlets allowing premixed reactants to flow from the burner's inner and outer plena to the nozzle exit. Upstream of each plenum, a metallic mesh sits atop a bed of 1 mm diameter ceramic beads to (1) ensure sufficient premixing
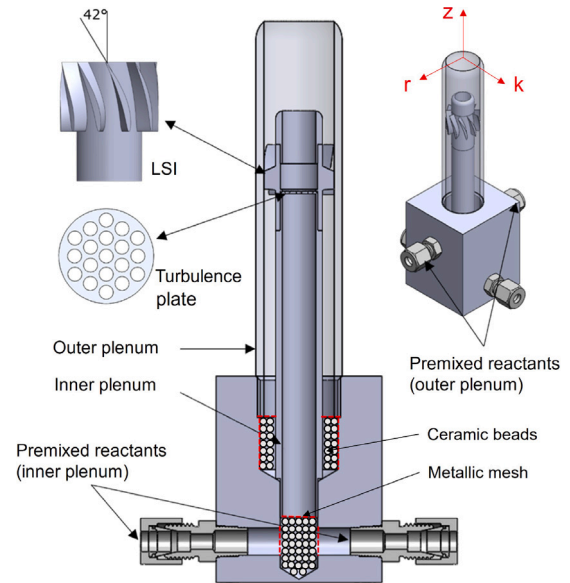

Fig. 2. Swirl burner: (a) cross-section side view, (b) 3-D metal-printed swirl injector, (c) turbulence screen and (d) isometric view. The r, z and k axes represent the radial, axial and azimuthal directions respectively (right).

of reactant air and fuel, (2) establish radial uniformity in the flow and, (3) serve as a flame arrestor in case of flashback. Reactants in the inner plenum flow through a turbulence plate (see Fig. 2) 10.2 mm in diameter with a hole diameter of 1.5 mm (i.e., blockage ratio of 59%) and produce a turbulent, *inner axial flow*. Reactants flowing through the outer plenum pass through a 3-D metal-printed annular swirler and produce an *outer swirling flow*. The swirler is composed of 10 vanes, each angled at 42°, with outer and inner diameters of 21.6 mm and 10.4 mm, respectively. The low-swirl injector is recessed 31.6 mm from the outer exit nozzle of the burner. The geometric swirl number (S) for each condition is computed by Eq. (6) [29]:

$$S = \frac{2}{3}\tan\theta \frac{1 - R^3}{1 - R^2 + [m^2(1/R^2 - 1)^2]R^2} \tag{6}$$

Here, θ represents the vane angle, R the radius ratio between the inner plenum and outer plenum, and m the mass flux ratio between the center jet and swirling flow. The presence of two independent plena allows for control of the flow split, characterized by m, between the inner turbulent flow and the outer swirling flow as a means to maintain a constant swirl intensity for each condition. The swirl burner was modular in design such that the turbulence plate, inner nozzle, and swirler were interchangeable. Reactant air and fuel flow rates were calculated per the lean combustion reaction equation outlined in [17] and were controlled using SLA Brooks mass flow controllers through a LabVIEW program developed in-house.

2.2. Experimental conditions

CH$_4$-air mixtures were enriched with H$_2$ in 20% increments by volume (X_{H_2}) in order to observe the gradual influence of flame stretch caused by differential diffusion on the turbulent burning rate. A sweep at a geometric swirl number $S = 0.6$ at constant laminar flame speed ($S_L^o = 0.267$ m/s) and constant bulk velocity ($U_{av} = 13$ m/s) was evaluated to solely highlight the influence of the local stretch factor on the turbulent burning rate, highlighted in Table 1.

Here, the diffusive flame thickness δ_L is defined by $\delta_L = \alpha/S_L^o$, where α is the thermal diffusivity of the mixture [30]. The integral length scale is calculated from the $X_{H_2} = 80\%$ condition [17] considering reactants flowing downstream of nozzle exit are well captured in the laser sheet's
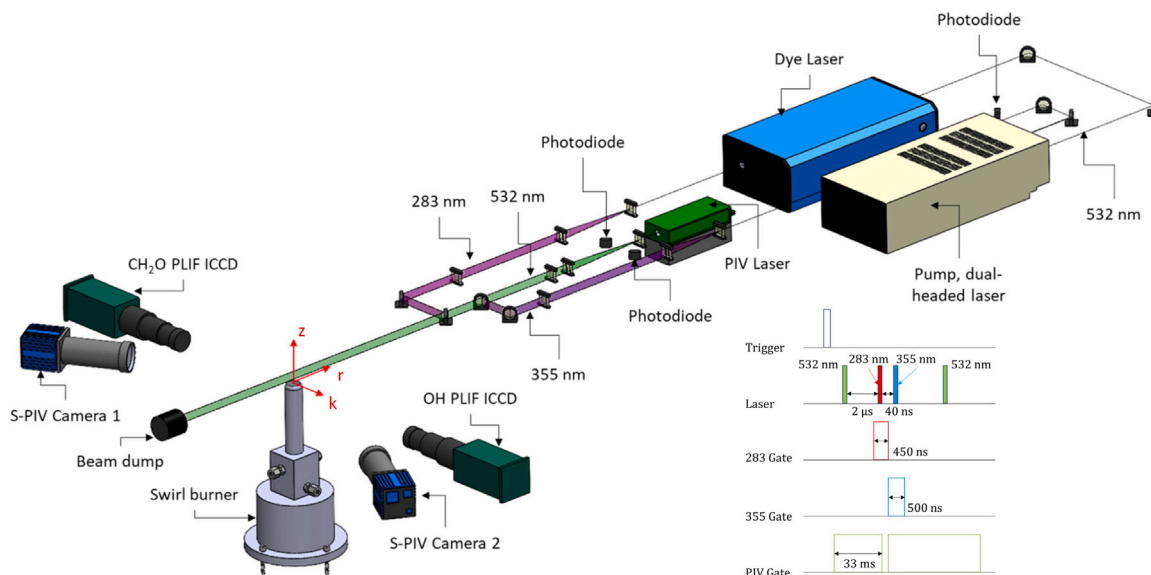
Fig. 3. PLIF/S-PIV systems and diagnostics with time chart, where *r*, *z* and *k* axes represent the radial, axial and azimuthal directions respectively.

Table 1
Conditions evaluated at constant S_L^o = 0.267 m/s, constant U_{av} = 13 m/s and constant S = 0.6 (i.e. flow split between outer and inner plenum is 82.5%-to-17.5%) at NRC and McGill University. X_{H_2} = 100% achieved in laboratory, but not listed here.

X_{H_2}	ϕ	Le_{eff}	Λ/δ_L	u_{RMS}/S_L^o	T_{ad} (K)
0	0.80	0.999	10.04	5.89	1938
20	0.75	0.862	10.11	5.69	1892
40	0.70	0.725	10.15	5.79	1832
60	0.64	0.587	10.22	5.84	1757
80	0.56	0.450	10.25	6.11	1657

FOV at this condition. The integral length scale is calculated in a 2-D rectangular region with a width equal to the diameter of the inner plenum (i.e., from $-0.23D_{nozzle}$ to $0.23D_{nozzle}$) and a height upstream of the flame (i.e., at mean progress variable $\bar{c}$ = 0.1). An average integral length scale in this region was calculated to be Λ = 3.14 mm, and is normalized by the diffusive flame thickness δ_L for each condition (see Table 1). This value is indicative that turbulent eddies grow from a 1.5 mm TGP hole diameter given the swirler's recess length from the nozzle exit. The mean three-component (3C) RMS velocity was also approximated in this region for each experimental condition as a measure for calculating the turbulence intensity of each condition. The Lewis numbers for pure fuel blends were also computed in Cantera such that an *effective* Lewis number could be defined for all fuel-blends on a volumetric basis [31,32]:

$$Le_{eff} = (1 - X_{H_2})Le_{CH_4} + X_{H_2}Le_{H_2} \tag{7}$$

Here, the Lewis numbers for 100% CH_4 and 100% H_2 are 0.999 and 0.447, respectively. All mixture and thermodynamic properties were computed in Cantera using the GRI-Mech 3.0 thermochemical reaction mechanism using P_{in} = 1 atm (101.3 kPa) and T_{in} = 298 K as inlet references, coupled to a multi-component transport model while enabling Soret effect [33].

2.3. Laser diagnostics

Planar laser-induced fluorescence (PLIF) was used to obtain the 2D distribution of hydroxyl (OH) species in the flame, which is a good marker of the flame reaction zone [34] (see Fig. 3). The PLIF setup incorporates a dual-headed, Nd:YAG pump laser (Spectra Physics) and dye laser (Sirah PrecisionScan). The pump laser delivers two laser beams, one of which is frequency-doubled (532 nm). The 532 nm

beam passes through the dye laser (dye medium is Rhodamine 6G) and frequency-doubled to 283 nm in order to excite the A-X (v'=1,v"=0) transition of OH at an average energy of 5 mJ/pulse. The OH laser beam was formed into a laser sheet where the shot-to-shot energy was recorded in real-time with photodiodes (ThorLabs) and was measured using a LeCroy oscilloscope (Wavesurfer 510). The OH fluorescence is captured with an intensified CCD camera (PIMAX 2, Princeton Instruments) with a projected spatial resolution of 90.9 μm/pixel. The OH camera was fixed with a UV lens having a focal distance of f = 105 mm and $f\#$ = 4.5, and equipped with a bandpass filter (center wavelength 320 ± 20 nm). The raw OH images were normalized by shot-to-shot variations in laser energy and mean laser profile according to standard methods [35]. Raw images were also corrected for mean background intensity to filter any reflection from the opposing camera lenses as well as additional background noise (i.e., S_{dark}). Corrected OH images were median filtered (7×7) according to the procedure developed by An et al. [17].

Stereoscopic particle image velocimetry (S-PIV) was used to calculate the two-dimensional, three-component (2D-3C) velocity field of each flame condition. The S-PIV setup incorporates a double-pulse, Nd:YAG laser (Twins CFR PIV200), delivering a pair of laser beams at 532 nm, which straddle the PLIF pulses and are time delayed between 5–30 μs depending on the bulk velocity of the condition. The 532 nm laser beam was formed into a 38 mm tall, collimated sheet, coincident with the PLIF laser sheets. Solid Al_2O_3 particles (~ 1 μm diameter) were seeded in the inner axial and outer swirling flows, where each plena was equipped with particle seeders manufactured in-house. Two CMOS cameras (LaVision Imager sCMOS) calibrated with a dot target (Type 106-10, from LaVision) were used to capture the Mie scattering signals from the solid particles and were arranged at an angle of 150° to satisfy the Scheimpflug condition [36]. The PLIF and S-PIV laser systems were triggered using a LaVision timing unit (PTU) and a delay generator (DG645). The cameras imaged a field-of-view (FOV) of approximately 76 mm × 64 mm with a projected spatial resolution of 34.1 μm/pixel. Velocity field vectors were calculated in DaVis 8.4 (LaVision software) from the spatial cross-correlation of consecutive PIV images, where a final interrogation window pass 32 × 32 pixels in size was used at an overlap of 50%. This led to a vector resolution of 0.55 mm/vector and a PIV spatial resolution of 1.1 mm, considering independent velocity vectors. The PLIF and S-PIV laser systems were triggered using a LaVision timing unit (PTU) and a delay generator (DG645) such that the 283 nm laser beam fired 2 μs after the first PIV pulse. The timing
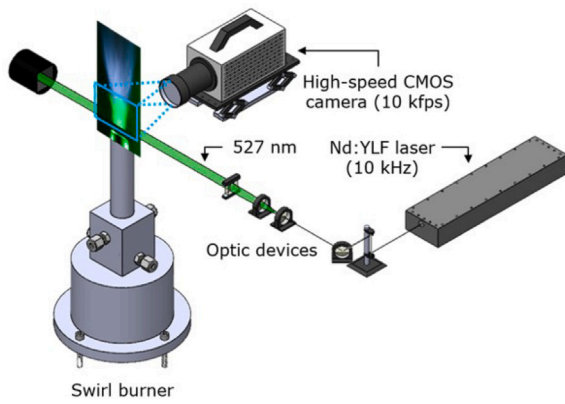
Fig. 4. High-speed particle image velocimetry (PIV) setup at McGill University.

of each laser pulse was monitored using the oscilloscope to ensure Mie signals would not conflict with fluorescence signals. Any axial (z-direction) adjustments to the burner were controlled via LabVIEW using a three-axis traverse to ensure the flame is appropriately imaged in the PLIF/PIV FOV, where raw images for each data set were acquired at a rate of 2 Hz.

High-speed particle image velocimetry (2D-PIV) was used to time-resolve the turbulent flow field at a repetition rate of 10 kHz (see Fig. 4). The experimental setup incorporates a single-head, diode-pumped Nd:YLF laser (Photonics DM20-527), delivering a green laser beam at 527 nm. The laser beam was formed into a collimated sheet able to sufficiently capture the flame surface for all levels of hydrogen enrichment. Oil aerosol of approximately 1 μm diameter in size was seeded in the inner axial flow from an oil droplet generator (TSI 9307-6). Air flowing through the inner plenum was redirected to the atomizer by means of a micrometer-controlled bypass, which allows a set amount of air to flow through an array of Laskin nozzles which bubble the seed liquid (i.e., canola oil). The oil droplets are aspirated through the system and simultaneously mixed with the bypassed air in a mixing tank downstream of the atomizer. A high-speed CMOS camera (Photron Fastcam SA5) was used to record particle Mie scattering at 10 kfps. The high-speed camera was equipped with a 105 mm lens (AF Micro Nikkor, $f\# = 2.8$) and focused to a spatial resolution of 29.5 μm/pixel (33.9 pixel/mm). The camera's spatial resolution was calculated from the negative image of a Thorlabs 0.5 mm spacing (R2L2S3P3) distortion grid target. The resolution was computed by normalizing the actual 0.5 mm grid spacing by the imaged radial and axial pixel separation between grid dots. The FOV of the flame was calibrated manually using a 2-axis stage to radially align the center of the CMOS camera to the center of a Thorlabs graduated card placed atop the nozzle exit. For each image pair, a multi-pass, decreasing window, sequential cross correlation scheme was used to compute the pixel displacement field with a resolution down to a 32×32 pixel interrogation window size with 75% overlap. This scheme resulted in an interrogation window spatial resolution of 944 μm × 944 μm in physical coordinates. Although this is not enough to resolve turbulent eddies at the Kolmogorov scale ($O(l_K) \approx 10^{-5}$m), it is enough to resolve the energy-containing eddies responsible for bulk wrinkling of the flame (given the hole diameter of the turbulence generating plate $D_{hole} = 1.5$ mm).

2.4. Processing techniques

2.4.1. Estimation of FSA

The flame surface area (FSA) enhancement due to turbulence (A_T/A_L), which is nominally three dimensional, is estimated from a 2-D cross section along the centerline of the exit nozzle. While the FSA can be approximated as the length of the 2-D flame contour

multiplied by the thickness of the laser sheet, DNS studies have found this approximation underpredicts the area by roughly $\approx 25\%$ as it does not account for out-of-plane flame wrinkling [37].

Therefore, trends in FSA enhancement with hydrogen enrichment are instead evaluated from the ratio of flame lengths ($A_T/A_L \sim L_T/L_L$), which can be calculated from the 2-D flame contour. The 2D flame contours were estimated from both (1) the binarization of the OH fluorescence signal and (2) the vaporization point of the Mie scattered oil aerosol, depending on the experimental campaign. From OH fluorescence, the instantaneous flame length L_T is normalized by the mean flame length L_L, calculated from the mean progress variable $\bar{c}$ map and extracting the mean flame contour at $\bar{c} = 0.5$. The progress variable map is calculated for each flame condition, and is defined as:

$$c = \frac{T - T_u}{T_b - T_u} \tag{8}$$

In Eq. (8), T represents actual temperature, T_u represents temperature of unburnt reactants and T_b represents temperature of burned products. A mean progress variable of $\bar{c} = 0.5$ from OH fluorescence corresponds to a temperature range between 900–1100 K for all evaluated H_2-enriched conditions. However, it is not possible to extract the mean flame contour from Mie scattering tomography since the vaporization of oil aerosol, $T_{vap,oil}$, occurs at a lower temperature. Ultimately, the instantaneous position of the flame front is approximated based on Mie scattering images where the position of the flame is defined by the isocontour at $T_{vap,oil} \approx 576$ K. For the flame conditions evaluated in this study, this corresponds to a reaction progress variable ranging between 0.3–0.35 depending on the CH_4/H_2 mixture. The individual flame instances are binarized and ensemble-averaged to obtain the mean progress variable $\bar{c}$ map, from which the laminar flame length L_L is extracted at $\bar{c} = 0.5$. The ratio L_T/L_L will be denoted as A_T/A_L throughout the remainder of the text for simplicity.

2.4.2. Measurement of S_u, S_{flame}, and S_f

The local flame displacement velocity S_f is resolved by tracking the approximate flame surface from the Mie scattered PIV image. The vaporized oil aerosol delineates the flame zone region between unburned reactants and burnt products. This region is tracked as a continuous contour using Pavlidis' algorithm for neighboring pixels [38]. The resultant contour is comprised of grid points where each of the local flame displacement speed S_f components can be calculated. The convective velocity of the flow, S_u is captured from PIV techniques and represents the flow just upstream of the tracked flamefront. The lab reference velocity of the flame, S_{flame}, represents the motion of the flamelet itself. The summation of both components normal to the flamefront, as outlined in [30], describes the local flame displacement speed. The S_u velocity component is calculated from the projection of velocity vectors (calculated in DaVis) from each interrogation window onto the normal line ($S_u = S_{PIV} \cdot \mathbf{n}$) passing through the flame grid point of interest (see Fig. 5), and are weighted in their proximity to the normal line. The upstream velocity, characterized as the minimum velocity before acceleration due to thermal expansion, is computed from the average of the two weighted velocities nearest to the flame along the normal line. The average is taken considering the flame is prone to wrinkling from turbulence and the minimum convective velocity is not always well defined. The convective velocity is assigned a positive value if the incoming reactant velocity is pointed towards the flame and a negative value if pointed away from the flame. From this point on, normalizations of S_u, S_{flame}, and S_f by the unstretched laminar flame speed S_L^o will be denoted by S_u/S_L, S_{flame}/S_L and S_f/S_L, respectively.

The velocity of the flamelet in the lab frame, S_{flame}, is calculated by considering the motion of the flame through five successive flamefronts: two upstream of t_i at time t_{i-1} and t_{i-2}, and two downstream of t_i at time t_{i+1} and t_{i+2} (see Fig. 6) [15,16]. The flame grid point from one flamefront is correlated to an adjacent flamefront by an optimization
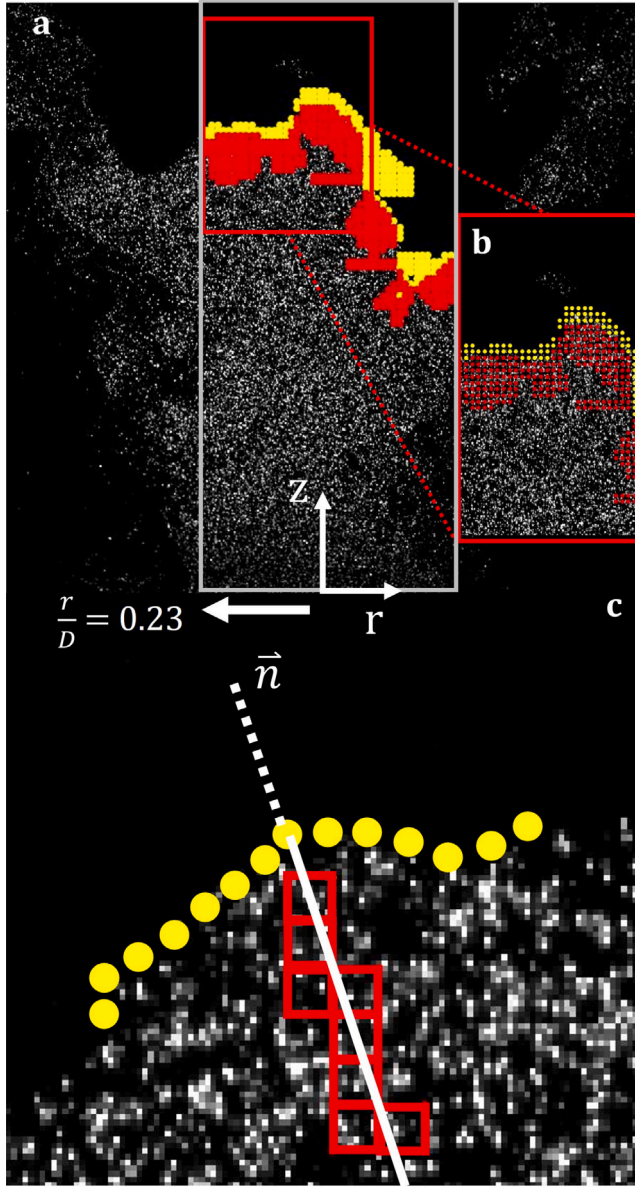
Fig. 5. (a) Measurement technique of S_u component of the local flame displacement velocity and, where red dots mark the corners of interrogation windows containing velocity vector data and yellow dots mark the approximate flame reaction zone (b) further zoomed-in to illustrate the sampling rate of calculation. (c) Schematic for the calculation of S_u at one flame grid point with the normal line in white. Test domain is delineated by gray rectangle, with a width of $r/D = 0.23$. (For interpretation of the references to color in this figure legend, the reader is referred to the web version of this article.)

Fig. 6. (a) Schematic of measurement technique of S_{flame} component of local flame displacement speed. (b) Zoom-in of tracked flame motion through 5 successive flamefronts. The blue dots represent grid points for the flamefront at time t_i while purple grid points represent adjacent flamefronts at different time instances. (For interpretation of the references to color in this figure legend, the reader is referred to the web version of this article.)

scheme of the minimum distance between them. Two constraints are imposed on the trajectory of the grid point from one time instance to the other: (1) the path is assumed to follow four interconnected third-order polynomials and (2) the polynomials must intersect normally to the flamefronts. The velocity of the grid point from t_{i-2} to t_{i+2} is estimated using a fourth-order finite differencing scheme outlined below:

$$S_{flame} = \frac{\partial z}{\partial t}\bigg|_{t_i} \approx \frac{8(z_{t_{i+1}} - z_{t_{i-1}}) - (z_{t_{i+2}} - z_{t_{i-2}})}{12 \Delta t} \qquad (9)$$

The S_{flame} velocity component is considered positive if the flamelet propagates towards the incoming reactant flow and negative if propagating away from the reactant flow. There are several factors which
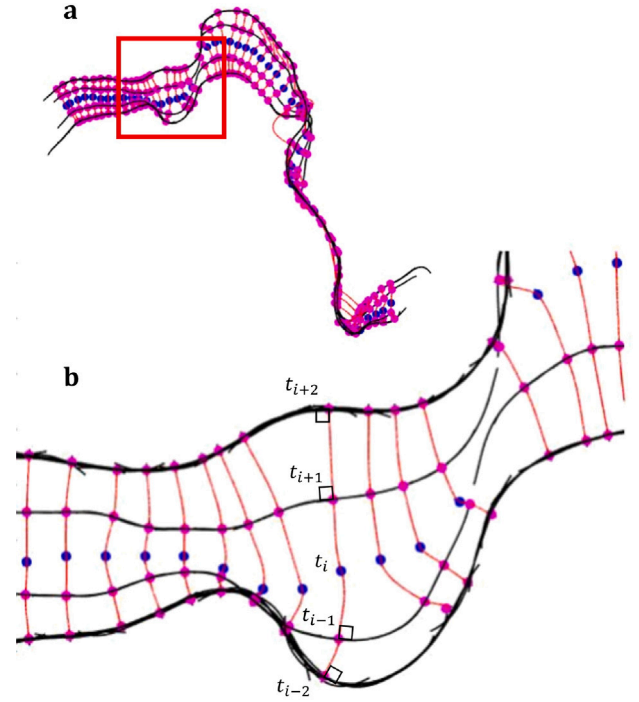
render successive flamefront tracking complex such as: flamefront wrinkling due to turbulence, disappearance of flame grid points in and out of the imaged FOV, and spurious velocities as a result of the flamelet moving too fast, resulting in erroneous tracking. To improve the efficiency of the algorithm, only a shortened region of the tracked flamefront was considered ($-0.23 D_{nozzle} \leq r \leq 0.23 D_{nozzle}$) while S_{flame} velocities exceeding the bulk velocity $\overline{U}$ were deemed non-physical.

Although high-speed PIV diagnostics are used to capture both velocity components of S_f, there is expected to be a bias due to unresolved, out-of-plane motion. Trends in 2-D S_f/S_L across CH_4-air mixtures with increasing hydrogen content are evaluated instead to provide a basis for studying the onset of differential diffusion effects. In reality, there is expected to be a bias of approximately 10%–20% by omitting out-of-plane motion [39]. However, given the flow conditions are consistent per condition, we also expect bias to be consistent among the conditions tested such that the observed trends are expected to hold.

2.4.3. Measurement of stretch components: κ and $K_{s,t}$

The components of the flame stretch rate, K are also extracted locally along the flamefront. The local curvature κ is calculated along the tracked flame surface contour with respect to flame coordinates (r, z), where r represents the radial direction, z represents the axial direction, while the prime and double prime of each flame coordinate function represents their first and second derivatives:

$$\kappa = \frac{r' z'' - z' r''}{(r'^2 + z'^2)^{3/2}} \qquad (10)$$

The local curvature is considered positive and negative if the flamefront is convex and concave towards the reactants, respectively. For uncertainties on local curvature, refer to Appendix A.

The hydrodynamic tangential strain rate $K_{s,t}$ (in units of s^{-1}) is defined by the change in tangential flow velocity nearest the flame, and is a component of the total flame stretch rate, K. In the same way
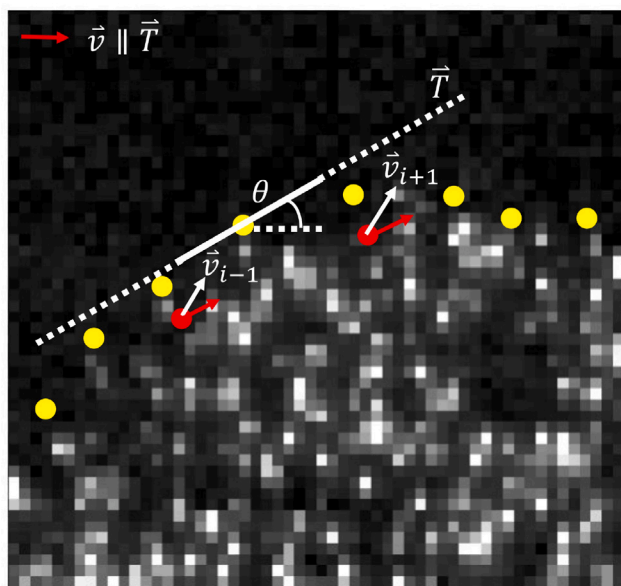
Fig. 7. Schematic for the calculation of the hydrodynamic tangential strain $K_{s,t}$ on a zoomed-in raw PIV image, for an arbitrary flame grid point.

that S_u considers the projection of velocity vectors onto the normal line passing through each flame grid point, the tangential strain rate considers the projection of velocity vectors onto its tangent line. The hydrodynamic tangential strain is calculated by considering the tangent slope at the flame grid point of interest P_i, which is obtained from flame surface tracking techniques. Knowing the angle of inclination of the tangent line (θ), the adjacent velocities near the flame grid point (at P_{i+1} and P_{i-1}) along the axial (z) and radial (r) directions are projected onto the tangent line vector by computing the inner product (see Fig. 7). The difference in projected velocities at P_{i-1} and P_{i+1} normalized by the distance between them results in the tangential strain at P_i. This algorithm for computing the tangential component of S_u is sampled at every 8 pixels along the flame contour, corresponding to the interrogation window overlap from PIV processing where velocity data exists. The hydrodynamic tangential strain is considered positive if there is an elongation effect in the following scenarios: (1) P_{i+1} exhibits larger rightward tangential velocity than P_{i-1}, (2) P_{i-1} exhibits larger leftward tangential velocity than P_{i+1} or (3) P_{i-1} and P_{i+1} exhibit tangential velocities outward from each other. Conversely, the hydrodynamic strain is negative in opposite scenarios, such that the flame experiences compression as a result of its change in tangential velocity. The local flame stretch rate K is the summation of $K_{s,t}$ and κS_{flame} at all flame grid points along the tracked flame surface contour.

3. Results and discussion

3.1. Flame and flow field characterization

The effects of hydrogen addition can be observed qualitatively from the instantaneous OH fields as the flame transitions from a 100% CH_4 to 20%CH_4/80%H_2. It is evident from the different axial positions of the low-swirl mixtures in Fig. 8 that H_2 enrichment causes the flame to stabilize closer to the nozzle exit. Considering the unstretched laminar flame speed S_L^o and the bulk velocity U_{av} are kept constant for each condition, the increased flame displacement must largely be a result of differential diffusion effects of H_2 compared to CH_4. The increasing turbulent flame speed with the upstream motion of the flame is consistent with the momentum balance in Eq. (4). It is important to note that, although the geometric swirl number in these cases ($S = 0.6$) is a theoretical limit between a low-swirl and high-swirl flame [28],

the flow field can still be considered low-swirl due to the absence of a central recirculation zone from the overlaid instantaneous PIV fields in Fig. 8. Therefore, low-swirl flame theory suggests that if the flame displaces upstream towards the burner, then the local flame displacement velocity must also be increasing due to its response to flame stretch, which changes with fuel composition.

Consequently, flame stretch sensitivity becomes an important parameter in predicting the turbulent flame speed, as outlined in Eq. (2). The influence of flame stretch is evident qualitatively from the instantaneous OH fluorescence. For instance, a pure CH_4 flame ($X_{H_2} = 0\%$) is primarily shrouded by the inner shear layer of the swirling flow. However, at larger volume fractions of hydrogen, the flame advances further into the shear layer (see Figs. 8 and 20), which can likely be explained by hydrogen's higher extinction strain rate [17]. Furthermore, this increased corrugation occurs simultaneously with the formation of cellular structures in the central non-swirling flow, exhibiting sharper positive local curvatures. The stronger normalized OH fluorescence signal at the forefront of the flame also suggests a strong response in local burning due to differential diffusion. Furthermore, comparing the OH fluorescence fields between 0% H_2 and 40% H_2 fraction and between 40% H_2 and 80% H_2 suggests that differential diffusion effects on flame structure reach a point of criticality somewhere between 40% H_2 and 80% H_2. These observations are sufficient enough to investigate the influence of flame stretch due to differential diffusion effects on the flame surface area (FSA) enhancement and the local flame displacement speed, S_f, as a result of increasing H_2 content.

Turbulent flame speeds in H_2-enriched mixtures have been approximated in low-swirl flames [40] by calculating the convective velocity at the flame leading edge. In this respect, an initial approximation of the increase in turbulent flame speed can be made from the S-PIV diagnostics setup, which allows for the convective velocity (S_u) determination upstream and downstream of the flame. Here, the axial velocity profile normalized by the bulk velocity is calculated along an isoline passing through the leading point of the flame (i.e., most forward tip of the W-shape, see Fig. 20 in Appendix C). The velocity profiles of the turbulent low-swirl flames are plotted in Fig. 9, where the lowest point of the profile before thermal expansion corresponds to an approximation on the turbulent flame speed ($S_{f,approx.}$).

As expected, the velocity profiles of the low-swirl flame demonstrate the same behavior as that observed from the instantaneous OH fields for increasing H_2 content, where each red marker depicts $S_{f,approx.}$ increasing in magnitude with increasing H_2% while also shifting upstream to an axial position closer to the nozzle exit.

3.2. Instantaneous A_T/A_L and local S_f statistics

A consequence of differential diffusion is the flame's sensitivity to stretch, K, which enhances wrinkling along the flamefront and as a result, increases FSA. The enhanced FSA with increasing H_2% leads to the consumption of more reactants, thereby increasing the turbulent burning rate. Although Eq. (4) is used a priori to infer an increasing turbulent flame speed from the instantaneous OH fields, observations of the instantaneous FSA and local flame displacement speed S_f provide a better characterization for increases in the turbulent burning rate. The FSA enhancement due to differential diffusion can be captured from OH fluorescence in Fig. 10(a) and Mie scattering in Fig. 10(b) in a probability density function (PDF). As expected, the PDFs exhibit higher probabilities for larger A_T/A_L as X_{H_2} increases, synonymous with a decreasing effective Lewis number. It is important to note that the PDFs from Mie scattering consider a dataset of 10,000 frames compared to 520 frames from OH PLIF, which plays a role in the degree of scatter of the data. Nevertheless, the rightward shift in PDFs from both experimental campaigns is in good agreement with qualitative observations. Furthermore, PDFs of A_T/A_L from OH PLIF also exhibit larger standard deviations than those collected from Mie scattering (i.e., higher probabilities for $A_T/A_L > 4$). This difference
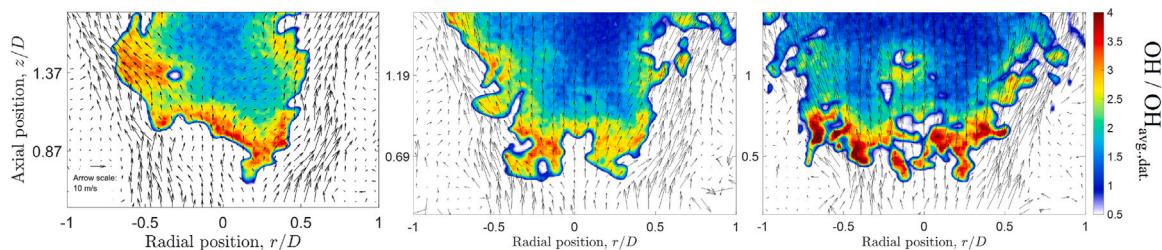
Fig. 8. Simultaneous OH and PIV instantaneous fields for swirl number $S = 0.6$ and $U_{av} = 13$ m/s at (a) $X_{H_2} = 0\%$, (b) $X_{H_2} = 40\%$ and (c) $X_{H_2} = 80\%$. Values along y-axis represent normalized axial distance relative to nozzle exit. OH fluorescence normalized by the average pixel intensity within the H_2 dataset.
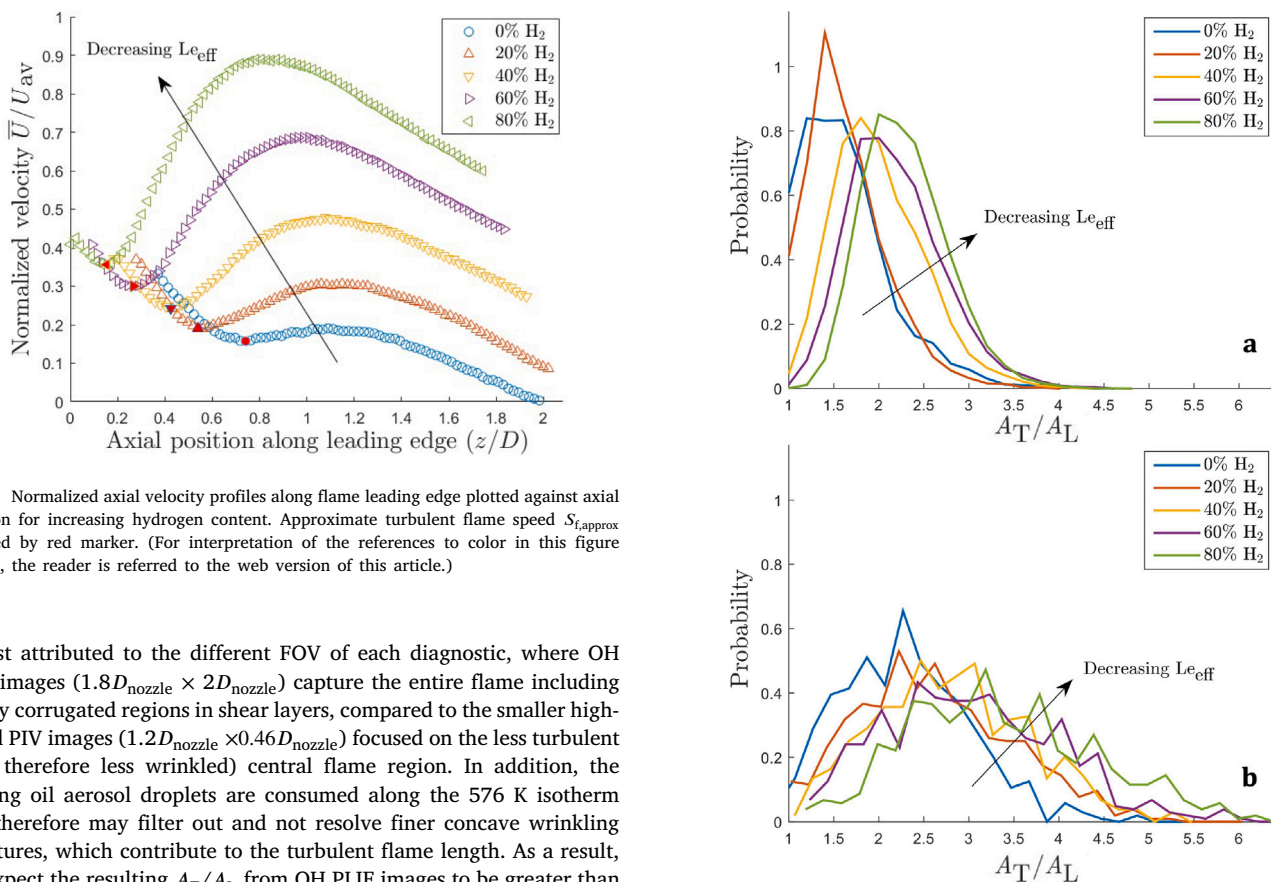

Fig. 9. Normalized axial velocity profiles along flame leading edge plotted against axial position for increasing hydrogen content. Approximate turbulent flame speed $S_{f,approx}$ denoted by red marker. (For interpretation of the references to color in this figure legend, the reader is referred to the web version of this article.)

Fig. 10. PDFs of FSA enhancement A_T/A_L for increasing hydrogen enrichment from (a) Mie scattered tomography and (b) OH PLIF.

is first attributed to the different FOV of each diagnostic, where OH PLIF images ($1.8D_{nozzle} \times 2D_{nozzle}$) capture the entire flame including highly corrugated regions in shear layers, compared to the smaller high-speed PIV images ($1.2D_{nozzle} \times 0.46D_{nozzle}$) focused on the less turbulent (and therefore less wrinkled) central flame region. In addition, the seeding oil aerosol droplets are consumed along the 576 K isotherm and therefore may filter out and not resolve finer concave wrinkling structures, which contribute to the turbulent flame length. As a result, we expect the resulting A_T/A_L from OH PLIF images to be greater than that of the high-speed PIV images for equivalent flame conditions.

Flame stretch sensitivity is also reflected in the normalized stretched flame speed S_f/S_L and is hypothesized to be largely influenced by hydrogen's preferential diffusion towards the flame's leading points. Therefore, calculation of the local flame displacement speed S_f from both S_u and S_{flame} components along the flamefront provides insight into the degree with which differential diffusion enhances propagation behavior. However, because the swirling flowfield is highly three-dimensional, instances such as flame turning and flame jumping (shown in Figs. 21 and 22 respectively) lead to numerical artifacts in the successive tracking of flamelet motion in consecutive instantaneous images, and are difficult to resolve consistently along the entire flamefront (see Figs. 21–22 in Appendix D). For simplicity, S_f is determined only at the most forward propagating (i.e., leading) flame grid point where flamelet motion can be reliably and robustly resolved. The PDFs of S_u and S_{flame} are plotted in Fig. 11. Therefore, in a low-swirl burner, flow divergence due to swirl leads to a reduction in average axial velocity downstream from the nozzle exit (see Fig. 9). Furthermore, the increased average value of S_u observed in Fig. 11 is consistent with flame stabilizing further upstream where the average bulk velocity, U_{av}, is higher.

However, the PDFs of S_{flame} are showcasing a more complex phenomenon. Fig. 12 highlights several phenomena from the evolution of five successive flamefronts: (1) flame "pinching" as a result of discontinuous oil aerosol pockets, (2) flame "turning" as a result of the flamefront moving left or right and (3) "flame jumping" as a result of the vaporization of oil aerosol upstream of the flame. As illustrated from the grid point tracking along the centerline (blue) and leading edge (red) of the flame, the phenomenon of flame jumping occurs much more frequently and prominently for higher hydrogen-enriched conditions (see examples (c) and (d) in Fig. 12). Such occurrences are well characterized by the PDFs of the S_u and S_{flame} components of the local flame displacement velocity, S_f. For instance, the PDFs of the S_u velocity component along the leading point exhibit higher probabilities at larger values of S_u. Furthermore, in Fig. 12, the normalized axial position of tracked flame grid points between the $X_{H_2} = 0\%$ and $X_{H_2} = 80\%$ conditions also demonstrate a flame displacing closer to the nozzle exit where convective velocities (i.e, S_u) are faster. Conversely, there
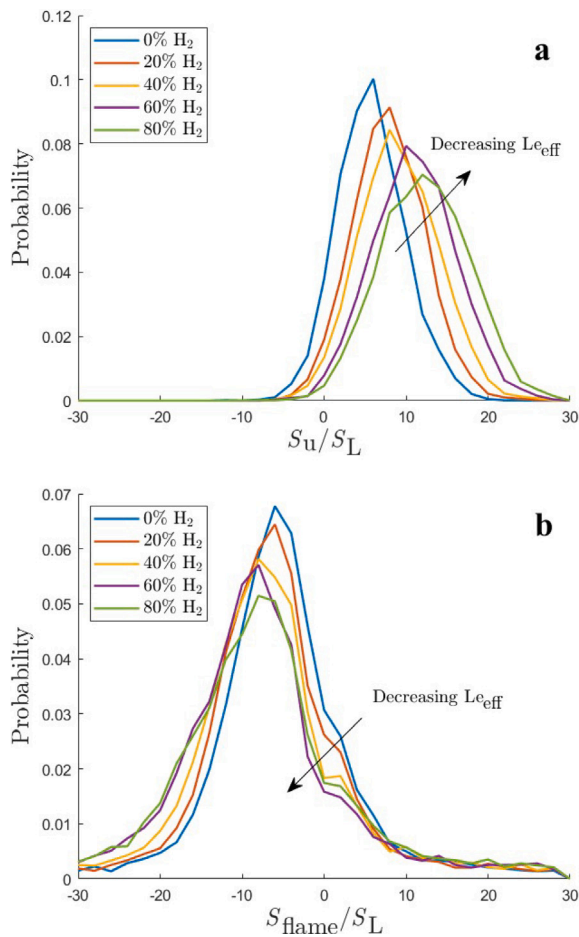
Fig. 11. PDFs of (a) the normalized local convective velocity of the flow S_u and (b) the normalized flamelet velocity S_{flame} at the flame's leading edge. Bin size is equal for both PDFs.

is not a marked shift of the S_{flame} PDFs towards positive velocities, but rather a slightly larger probability of negative S_{flame} values with H_2 enrichment. As observed from Fig. 12, tracking conditioned to the flame's leading edge (i.e. coordinate) demonstrates a flamelet moving away from the nozzle and then rapidly accelerating (or "jumping") towards the nozzle for the 80%H_2 condition, compared to the 0%H_2 condition, which appears more symmetric in its flamelet motion. With regards to the directional convention in computing S_{flame}, the flamelet moving away from the nozzle is assigned a "negative" S_{flame} velocity component and vice versa for "positive". Therefore, if there are more instances of the flamelet moving away with hydrogen enrichment, then the PDFs of S_{flame} will showcase this "negative" trend. In cases when a flamefront moves too quickly between consecutive images, the algorithm correlating one flamefront to the next results in a numerical artifact, as illustrated in Appendix D. In the case of flame jumping, where the flamefront slowly drifts away from the nozzle before rapidly accelerating towards the nozzle, flamelet motion S_{flame} is more likely to be better resolved for a flamefront moving downstream than upstream. The PDFs of S_{flame} highlight this trend, with a decreasing probability for positive S_{flame} values and increasing probability for negative S_{flame} values with hydrogen enrichment. The occurrence of flame jumping as a result of oil aerosol vaporization upstream could be due to faster swirling flow as the flame displaces closer to the nozzle exit (see Appendix D regarding this evolution with hydrogen enrichment). Nevertheless, the increasing probability for faster flamelet motion is to be expected, and suggests the flame displacement in response to hydrogen enrichment has an effect on both velocity components S_u and S_{flame}.

The summation of the S_u and S_{flame} velocity components at the flame leading grid point results in the PDFs of the normalized stretched flame speed $= S_f/S_L$ in Fig. 13. It is important to note that the velocity components S_u and S_{flame} used to determine S_f may be positive or negative according to the definition in Section 2. For example, a "negative" local S_f can occur if the flamefront motion S_{flame} moves downstream faster than the incoming convective velocity, S_u. While this scenario is possible, the PDFs of S_f/S_L illustrate a higher probability for larger stretched flame speeds with a decreasing effective Lewis number. Essentially, the increased stretch sensitivity illustrates how differential diffusion enhances the local propagation velocity and the local burning rate in mixtures with increasing X_{H_2}. As seen in Fig. 13, the mean value of S_f/S_L for $X_{H_2} = 0\%$ is 3.24 while for $X_{H_2} = 80\%$, S_f/S_L more than doubles to 7.81. Using our definition for the turbulent flame speed at isosurface A_T, S_f measured at an effective progress variable of $\bar{c} \approx 0.3$–0.35 increases by a factor of 2.4 from 0% to 80% X_{H_2}. This is comparable to the increase in the approximate turbulent flame speed $S_{f,approx}$ at an effective progress variable of $\bar{c} = 0.1$ by a factor of 2 (see Fig. 9). The increase in hydrogen fraction from 0% to 80% X_{H_2} also leads to an increase in FSA generation, A_T/A_L, by a factor of 1.4 [41].

Furthermore, the relative contribution between flame stretch sensitivity and FSA generation in response to hydrogen enrichment is plotted in Fig. 14, such that the averaged S_f/S_L (i.e., mean of S_f PDFs) is weighted by the averaged FSA enhancement (i.e. mean of A_T/A_L PDFs) for each evaluated H_2 condition. Their relative contribution demonstrates a consistent increase with hydrogen enrichment, where $\langle S_f \rangle /S_L$ is the dominant mechanism behind an increasing turbulent burning rate. This relationship between $\langle S_f \rangle /S_L$ and $\langle A_T \rangle /A_L$ is particularly revealing considering the onset of differential diffusion effects become prominent between 40% to 60% hydrogen fuel volume fraction. What is very interesting is that, in Fig. 14, we see that $\langle S_f \rangle /S_L$ increases faster than $\langle A_T \rangle /A_L$ as Le_{eff} decreases, suggesting that differential diffusion acts more to increase the local burning rates than by increasing flame surface area after some critical Lewis number. In response to hydrogen enrichment and a decreasing effective Lewis number, an average contribution between both $\langle S_f \rangle /S_L$ and $\langle A_T \rangle /A_L$, is $\approx$ 2.6. Roughly, this equates to a 72% contribution on turbulent burning rate enhancement from stretched flame speeds compared to 28% from FSA generation. The relative contribution determined in this study from hydrogen enrichment in low-swirl flames is in good agreement with the similar work of Abbasi-Atibeh et al. on differential diffusion effects in counterflow flames [15,16,31]. This finding suggests that there may be a universal relationship to predict turbulent burning rates as a function of differential diffusion across various burner geometries for low-Lewis number mixtures. Although the stretch factor and turbulent burning rate cannot directly be inferred since S_C and Σ_{max} cannot be obtained in this study, I_o and Σ will ultimately be proportional to the increase in both S_f/S_L and A_T/A_L, respectively.

3.3. Local K and local κ statistics

In low-Lewis number mixtures, the flame stretch rate K becomes the mechanism responsible for enhancing the turbulent burning rate and contributes to an increasingly corrugated flamefront. In an effort to understand the influence of differential diffusion on flame topology, the local curvature κ is extracted along the instantaneous flamefront. The curvature PDFs, plotted in Fig. 15, remain centered at zero curvature with an increasing standard deviation in response to hydrogen enrichment. The increasing standard deviation for a decreasing effective Lewis number is indicative of higher, but equal probabilities for positive curvatures to be balanced by negative curvatures. Examining the positive curvature from the PDFs in Fig. 15 demonstrates larger probabilities for higher values from $X_{H_2} = 40\%$ to higher hydrogen content. This transition towards larger positive curvatures with hydrogen enrichment reflects the transition point in the A_T/A_L PDFs towards
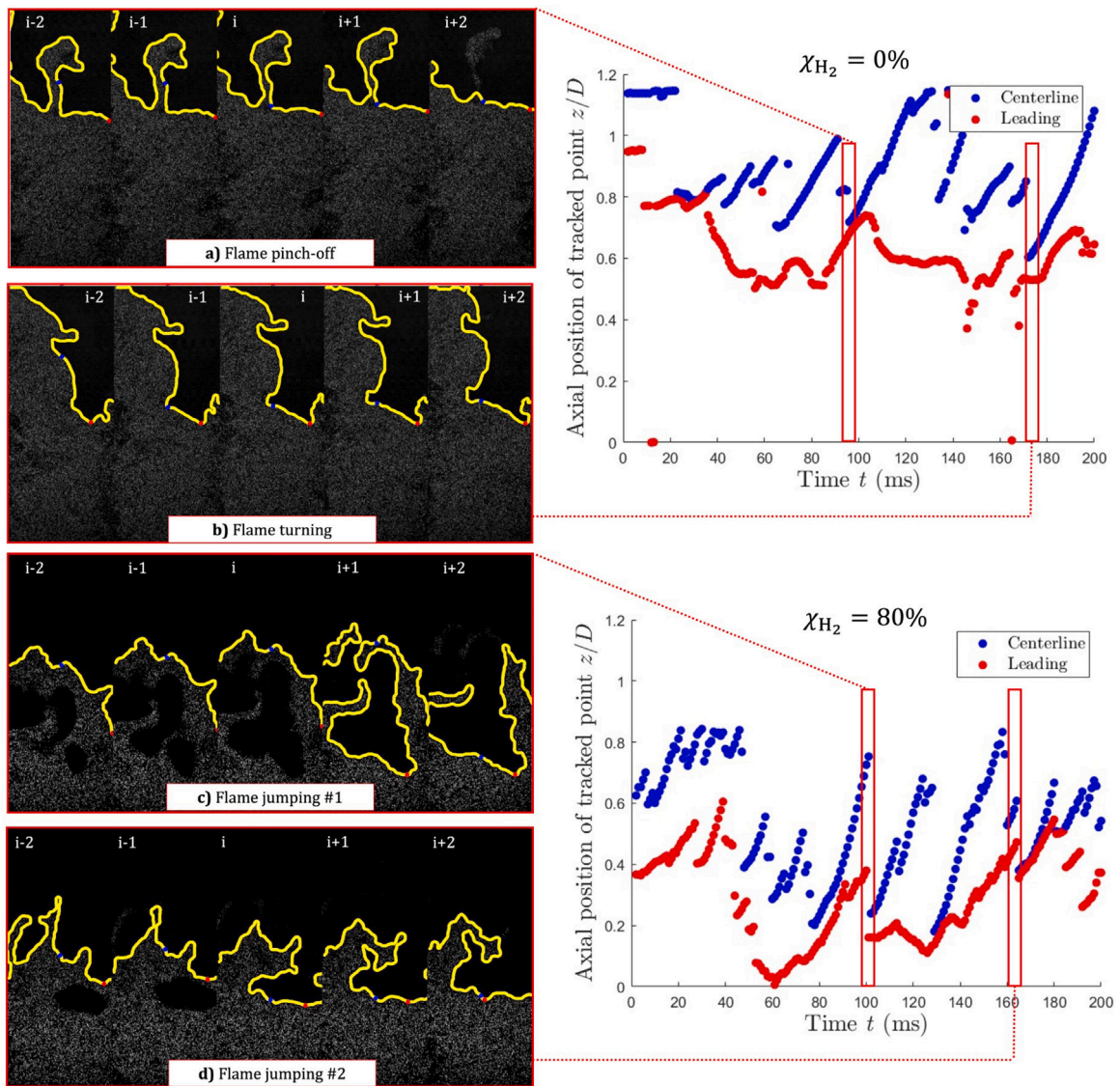
Fig. 12. Flame grid point tracking along centerline (blue marker) and leading point (red marker) for $X_{H_2} = 0\%$ (top) and $X_{H_2} = 80\%$ (bottom) conditions along with examples of time-resolved flame dynamics using high-speed PIV diagnostics: (a) flame "pinch off" resulting in drop in axial position along centerline, (b) flame turning, and (c) major and (d) minor flame jumping as a result of vaporization pockets upstream. (For interpretation of the references to color in this figure legend, the reader is referred to the web version of this article.)

larger values as the effective Lewis number decreases. This trend also suggests the existence of a critical Lewis number where differential diffusion phenomena become more pronounced.

The curvature component of the stretch rate, κS_f is also compared with the hydrodynamic strain rate component $K_{s,t}$ at the leading point in Fig. 16. The significant difference in stretch contribution can largely be explained by the combining curvature and local flame displacement speed response to hydrogen enrichment. Conversely, the hydrodynamic strain rate remains stagnant as a result of the constant U_{av} constraint maintained in each condition. The bulk velocity remaining constant suggests that the turbulent flow field does not contribute as significantly to flame stretch as increasing curvature does from the preferential diffusion of hydrogen. In this regard, differential diffusion arising from hydrogen enrichment persists in stretching the flame, at the turbulence intensity studied. The interplay between local curvature and increasing local flame displacement speed is also well summarized from the joint PDFs between the stretched flame speed and positive curvature at the leading points, shown in Fig. 17. At $X_{H_2} = 0\%$, S_f/S_L does not deviate far from unity for varying values of positive curvature while for the $X_{H_2} = 80\%$ condition, there is a mild increase for larger

S_f/S_L with increasing positive curvature. Nevertheless, the joint PDF of the $X_{H_2} = 80\%$ condition does not suggest that the most positive curvatures lead to the largest observations of the local flame displacement speed, as proposed by the theory of leading points. This occurrence is consistent with DNS studies conducted by Berger et al. [23] in a premixed, lean hydrogen–air flame, which also suggests increases in S_f/S_L do not largely occur in the positively curved regions of the flame, regardless if the mixture is thermodiffusively stable or unstable.

Similarly, in their study of thermodiffusively-unstable H_2/CO flames, Marshall et al. could not consolidate variations in the flame stretch rate at the leading points with variations in turbulent flame speeds [42]. Although the curvature component κS_f has been shown to globally increase in response to differential diffusion, decoupling κ and S_f in Fig. 17 demonstrates that the largest values of the local flame displacement speed do not always occur at the most convex regions of the flame. While the local flame displacement speed is evaluated consistently at the leading point, the leading point curvature varies much more significantly for larger % of H_2 enrichment. This suggests that the enhancement in turbulent flame speed and turbulent burning rate may simply be due to an increase in global curvature than
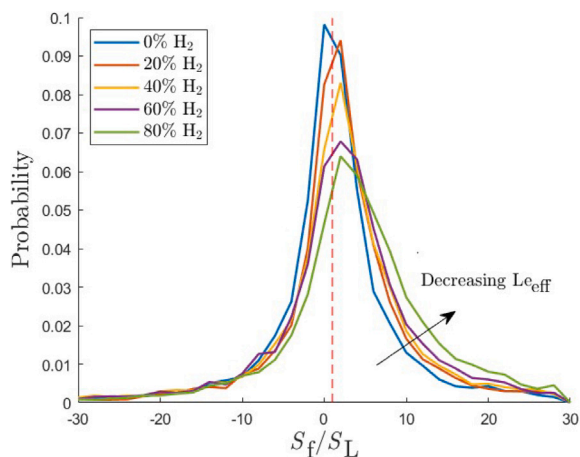
Fig. 13. PDFs of normalized stretched flame speed S_f/S_L at the flame's leading edge, with $S_f/S_L = 1$ marked by the red, dotted line. Bin size is equal to PDFs of S_u and S_{flame}. (For interpretation of the references to color in this figure legend, the reader is referred to the web version of this article.)
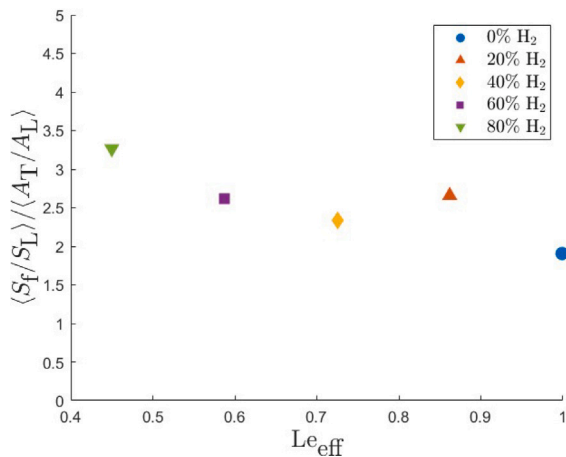

Fig. 14. Normalized stretched flame speed $\langle S_f/S_L \rangle$ at leading point weighted by mean FSA enhancement $\langle A_T/A_L \rangle$, correlated against effective Lewis number Le_{eff}.

Fig. 15. PDFs of global (a) curvature κ and (b) positive curvature $\kappa > 0$ along entirety of flamefront.

leading point curvature. In this manner, the relationship between local curvature and the stretched flame speed cannot be predicted solely by the leading points theory.

4. Conclusion

A thorough characterization of hydrogen combustion behavior is necessary for establishing a sustainable and renewable energy framework. The behavior of hydrogen–air mixtures is largely influenced by differential diffusion, and poses a challenge if hydrogen fuel is to be integrated at the industrial scale. This study examines the role of differential diffusion in lean, premixed H_2-enriched low-swirl flames through qualitative and quantitative analysis of its instantaneous OH fields, flame displacement speeds, and stretch rate statistics using PLIF and PIV laser diagnostics. The key results of this analysis are summarized by three findings:

(1) Low-swirl flames experiences a monotonically increasing, mean axial displacement towards the nozzle exit with hydrogen enrichment, caused by increasing turbulent flame speed even though the unstretched laminar flame speed is maintained constant. The increase in turbulent local consumption speed as a response to hydrogen enrichment in mixtures at constant unstretched laminar flame speed
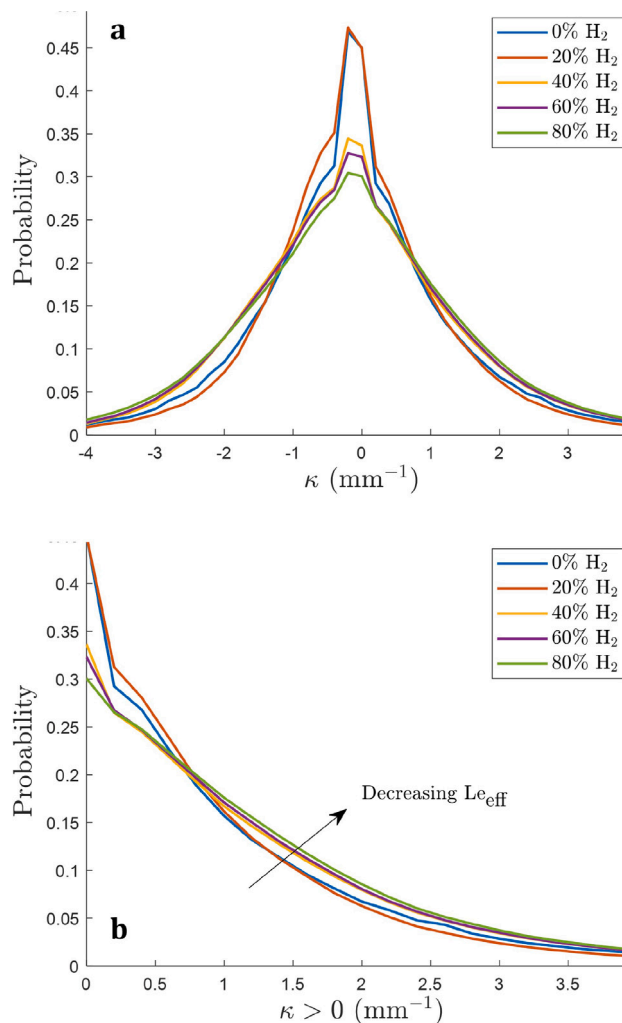
and near-constant turbulence intensity demonstrates the influence of differential diffusion.

(2) The relative contribution between the stretched flame speed and FSA enhancement has been correlated against the effective Lewis number. The average contribution between S_f/S_L and A_T/A_L has been found to be 72% and 28% respectively, similar to prior studies, suggesting there may be a consistent relationship to quantify the effects of differential diffusion.

(3) The primary control mechanism for increases in the local flame displacement speed and the turbulent burning rate suggests a stronger dependence on increases in global curvature than leading point curvature, contrary to the theory proposed on flame leading point dynamics.

While not the main outcome of this study, several dynamics, such as sudden flame acceleration ("jumping") and shear layer flame stabilization, outline the limitation of 2-D analysis in such turbulent conditions. As such, three-dimensional flame and flow characterization to resolve such phenomena are indeed of interest for future work.

CRediT authorship contribution statement

Benjamin Francolini: Conceptualization, Data curation, Formal analysis, Funding acquisition, Investigation, Methodology, Project administration, Resources, Software, Validation, Visualization, Writing – original draft, Writing – review & editing. **Luming Fan:** Resources,

Declaration of competing interest

The authors declare that they have no known competing financial interests or personal relationships that could have appeared to influence the work reported in this paper.

Data availability

Data will be made available on request.
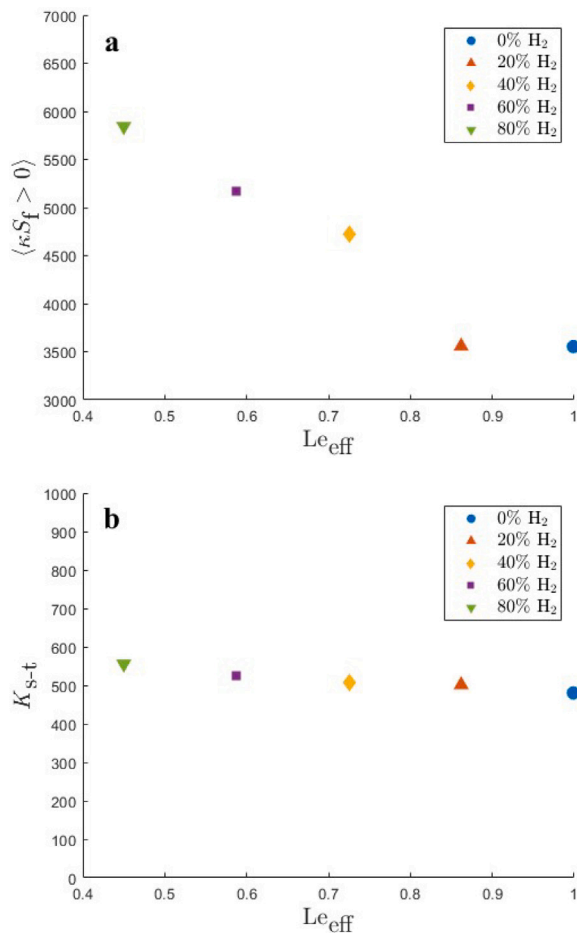
Acknowledgments

Fig. 16. At the leading point, (a) mean of the positive curvature component κS_{f} and (b) mean of the positive hydrodynamic tangential strain component $K_{\mathrm{s,t}}$ of the flame stretch rate K plotted against effective Lewis number, $\mathrm{Le}_{\mathrm{eff}}$. Note difference in scale on the y-axis of both plots.
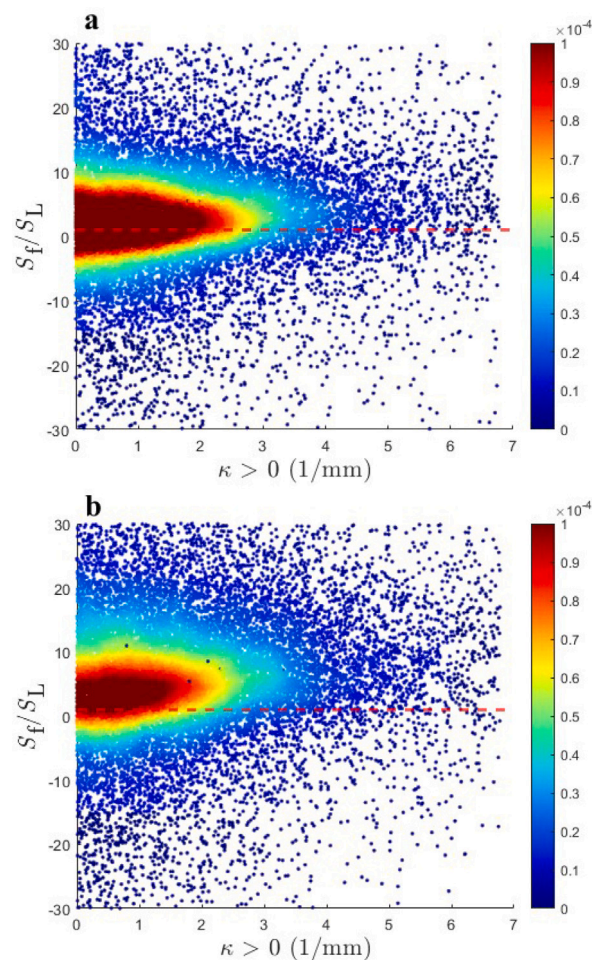

Fig. 17. Joint PDF of local flame displacement speed enhancement $S_{\mathrm{f}}/S_{\mathrm{L}}$ at the leading point correlated against positive curvature at the leading point for (a) $X_{\mathrm{H_2}} = 0\%$ H_2 and (b) $X_{\mathrm{H_2}} = 80\%$ H_2. Red-dotted line represents $S_{\mathrm{f}}/S_{\mathrm{L}} = 1$. Color map represents joint probability. (For interpretation of the references to color in this figure legend, the reader is referred to the web version of this article.)

Table 2
Summary of variable inputs in Monte Carlo analysis used in uncertainty quantification of local curvature κ from Mie scattered tomography.

Variables used for κ calculation	Distribution	Parameters	Limits
Binarizing factor	Random	$\mu = 0.5$	max/min = 0.45/0.55
Gaussian kernel	Random	$\mu = 7$	max/min = 6.3/7.7
Median filter kernel	Random	$\mu = 5$	max/min = 4/6
Uncertainty of spatial coordinates	Normal	$\mu = 0$	$\sigma = 29.5$ μm
Image magnification	Normal	$\mu = 1$	$\sigma = 0.007$
Image distortion	Normal	$\mu = 1$	$\sigma = 0.006$

Appendix A. Uncertainty on κ calculation

The uncertainty on local curvature calculation from high-speed Mie tomography has been performed for three distinct flame realizations at the $X_{\mathrm{H_2}} = 80\%$ condition using a Monte–Carlo (MC) analysis to produce 1000 distinct flame contours. The MC inputs are comprised in Table 2:

The raw PIV image is initially 2-D Gaussian filtered using a smoothing kernel with a standard deviation of $\sigma = 7$. The Gaussian filtered image is then binarized by a threshold of $\mu = 0.5$, for which the process iterates across the entire width of the frame. A 2-D Median filter with a nominal $[5 \times 5]$ window is then used to smooth rough edges from the binarized image, from which the flamefront is tracked and the
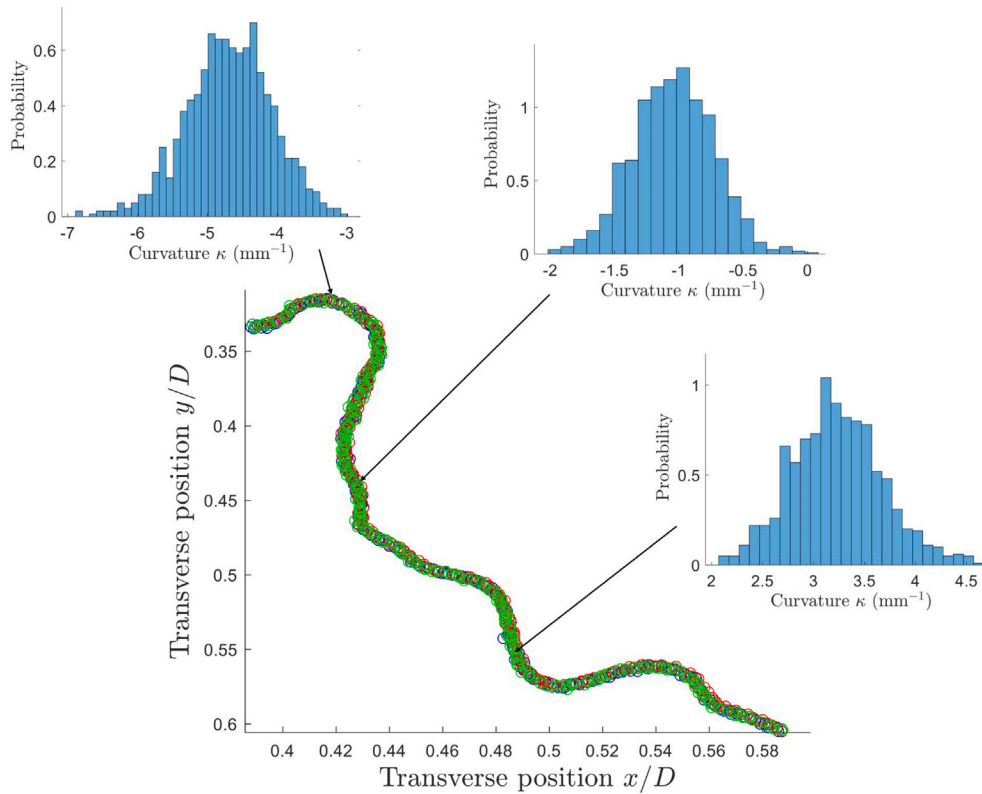
Fig. 18. Quantification of curvature uncertainty from Monte Carlo analysis. Open circles corresponds to flame contour produced from varying Monte Carlo thresholds within boundaries. Three sample contours are shown along with corresponding curvature PDFs at specified locations.
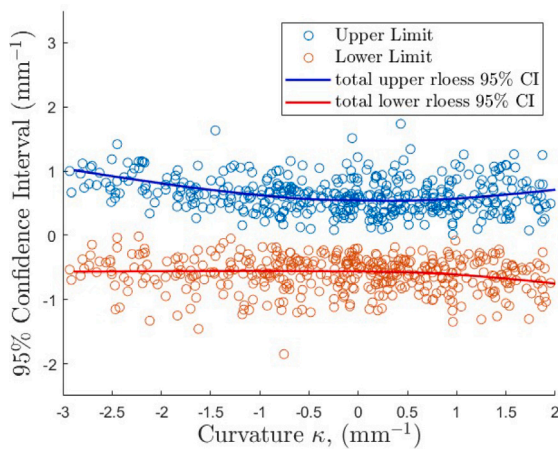

Fig. 19. Upper and lower 95% confidence intervals (circled) with robust LOESS fit (solid line) through data.

curvature is calculated. As the uncertainties in curvature propagate for an increasing number of image thresholds, an additional uncertainty on the spatial resolution was considered, such that flame coordinates along the MC contours are displaced following a normal distribution with $\sigma = 14.8$ μm (equivalent to 0.5 pixel at spatial resolution of high-speed PIV experiments). Lastly, an estimation is made on the curvature uncertainty due to image magnification ($\sigma = 0.007$) and distortion ($\sigma = 0.006$), assumed due to conversion of curvatures from pixel^{-1} to mm^{-1}. In this MC analysis, the input variables used in image thresholds were randomized between a minimum and maximum value relative

to the nominal value while median filtering was randomized between window sizes $[4 \times 4]$ to $[6 \times 6]$. The reference curvature is obtained along the reference flame contour using a fourth-order polynomial fit with 33 points. The Monte Carlo curvature is obtained by calculating the curvature at the location on the Monte Carlo contour with the closest Euclidean distance to the reference contour (see Fig. 18). Monte Carlo curvatures are calculated in intervals of 4 grid points along the reference contour.

From Fig. 19, the upper and lower 95% confidence limits are plotted from all three flame realizations and are fitted with a robust local regression fit ("RLOESS") with a 0.9 smoothing parameter value. The 95% confidence interval limits are smallest near zero-curvature and uncertainty begins to grow past ± 2 mm^{-1}. In general, the 95% confidence interval limits demonstrate the majority of curvatures lie within a 1 mm^{-1} uncertainty, illustrating that the fourth-order polynomial fit is sufficient in calculating curvature for the most hydrogen-enriched condition.

Appendix B. Uncertainty in flamefront tracking

The degree with which the MATLAB tracking algorithm predicts the flamefront location is subject to inherent uncertainties in post-processing, as detailed by Abbasi et al. [31]. Several sources of uncertainty between the predicted flamefront and the actual flamefront include the mean tracer particle distance l_p, the evaporation distance l_{evap} as a result of the oil droplet lifetime and uncertainties in distance due to median filtering l_{Filt} and size of the oil droplets captured by the CMOS camera l_I. The mean tracer particle distance, which coincides with the seeding density, is calculated from the binarized Mie scattered image relative to its equivalent saturated image such that l_p characterizes the average distance between particles. This average measurement
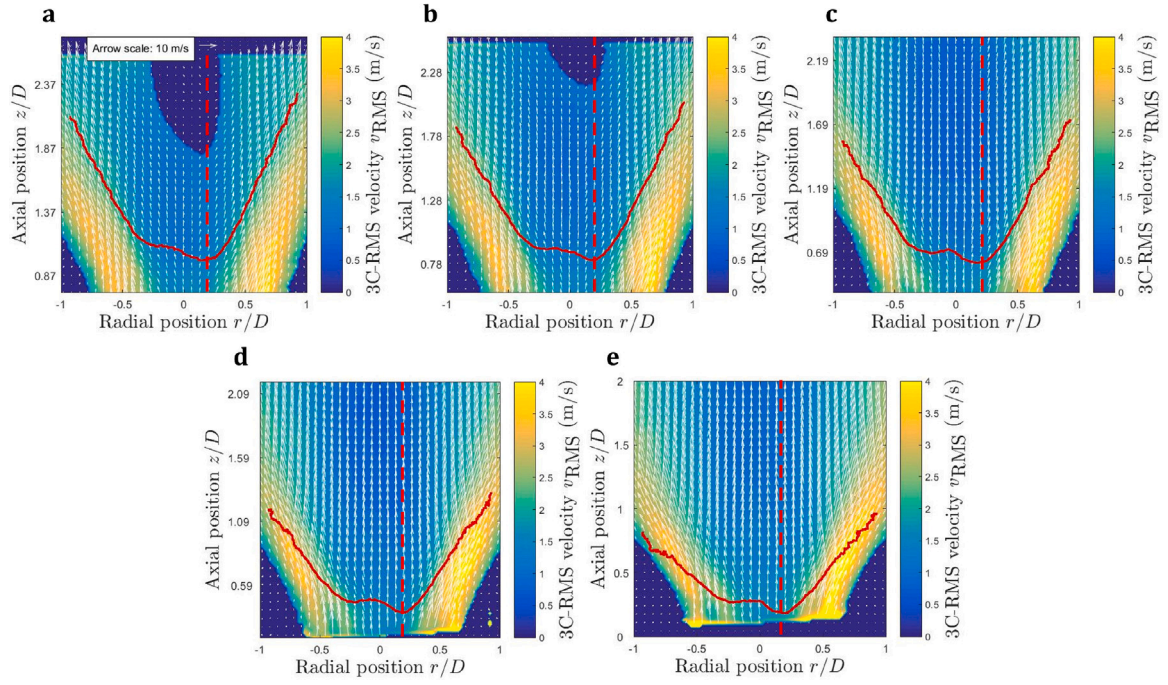
Fig. 20. Mean progress variable $\bar{c} = 0.1$ (red) overlaying 3-component RMS velocity field for (a) $X_{H_2} = 0\%$, (b) $X_{H_2} = 20\%$, (c) $X_{H_2} = 40\%$, (d) $X_{H_2} = 60\%$ and (e) $X_{H_2} = 80\%$ conditions. White vector field denotes mean axial velocity field for each condition respectively, down-sampled by a factor of 3. (For interpretation of the references to color in this figure legend, the reader is referred to the web version of this article.)
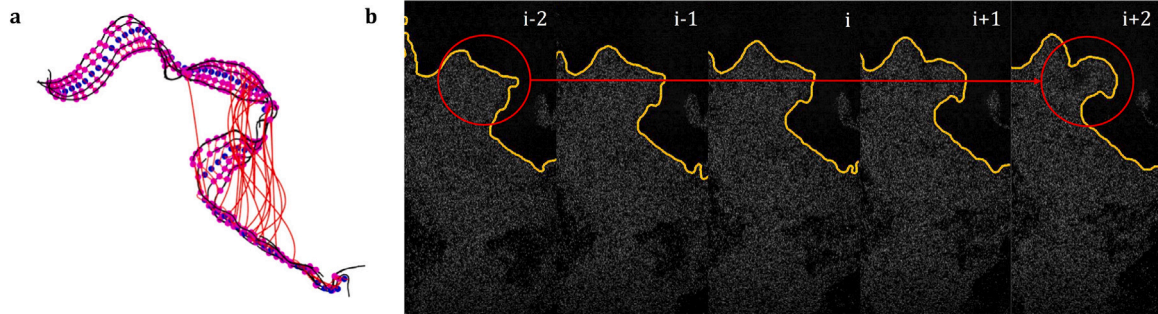

Fig. 21. Example of 5 successive flamefronts (t_{i-2} to t_{i+2}) depicting (a) inadequate tracking of flamelet motion due to (b) flame "turning" phenomenon. Example shown is of CH_4-air mixture ($X_{H_2} = 0\%$).

is performed for 2000 PIV images for all conditions evaluated. The oil evaporation distance l_{evap} is calculated from the multiplication of its lifetime τ_{evap} and the maximum flamelet velocity $S_{F,max}$ measured in post-processing. The oil lifetime is expressed as $\tau_{evap} = d_p^2/E$, where d_p is estimated to be at most ≈ 2 μm and E is the evaporation constant, as described in [43]:

$$E = \frac{8\lambda}{\rho c_p} \ln\left(1 + \frac{c_p(T_\infty - T_s)}{h_v}\right) \qquad (11)$$

Here, λ is the thermal conductivity of the mixture, ρ and c_p are the density and specific heat capacity of the canola oil, T_∞ is estimated as the average temperature between the adiabatic temperature and the ambient room temperature: $T_\infty = (T_{ad} - T_{amb.})/2$, T_s is the flash point of the oil at ≈ 576 K and h_v is the latent heat of vaporization of the oil. The distance uncertainty due to non-linear median filtering of the Mie scattered image with a 5×5 window is estimated as $l_{Filt} \approx 2.5$ pixels. Lastly, the distance related to the pixel width of the imaged particle on the CMOS array is estimated as $l_I \approx 2$ pixels. The uncertainties on l_{Filt} and l_I are converted to physical units through the spatial resolution coefficient, C. All uncertainty contributions to flamefront tracking are outlined in Table 3.

Table 3

Uncertainties in flamefront tracking dependent on mean particle distance l_p, evaporation distance $l_{evap.}$ and distances due to filtering $l_{Filt.}$ and imaging l_I of seed particles.

$l_{Tot.} = \sqrt{l_I^2 + l_{Filt.}^2 + l_p^2 + l_{evap.}^2}.$

X_{H_2}	l_I/δ_L	$l_{Filt.}/\delta_L$	l_p/δ_L	$l_{evap.}/\delta_L$	$l_{Tot.}/\delta_L$
0	0.189	0.236	0.589	0.041	0.663
20	0.190	0.237	0.472	0.042	0.563
40	0.191	0.238	0.442	0.043	0.539
60	0.192	0.240	0.387	0.046	0.496
80	0.193	0.241	0.335	0.049	0.458

Therefore, the total uncertainty due to flamefront tracking, which is calculated by the root of the sum of squares from all uncertainty components is estimated to be within 0.7 times the diffusive laminar flame thickness of the hydrogen-enriched mixture ($\leq 0.7\delta_L$).

Appendix C. Velocity field calculations

Fig. 20 illustrates the 3-C RMS velocity field for each hydrogen-enriched condition superimposed with the axial velocity field vector map. The dotted red line passes through the leading edge of the flame
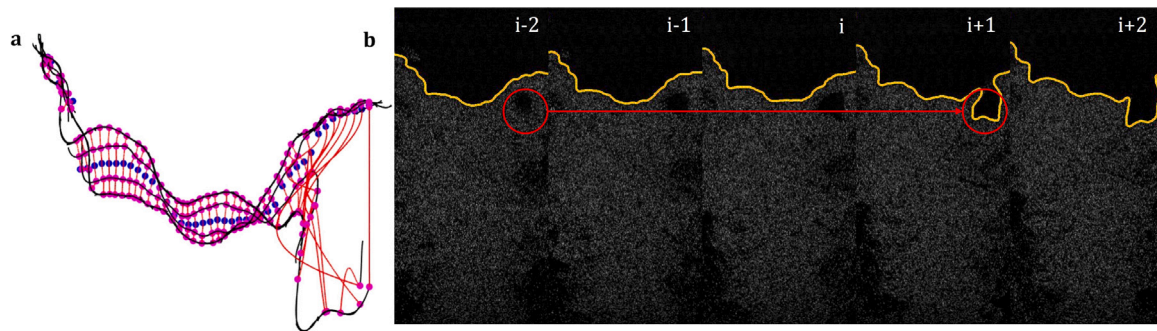
Fig. 22. Example of 5 successive flamefronts (t_{i-2} to t_{i+2}) depicting (a) inadequate tracking of flamelet motion due to (b) flame "jumping" phenomenon. Example shown is of CH$_4$-air mixture ($X_{H_2} = 0\%$).

surface, where a rough estimate is made on the turbulent flame speed. A mask is applied to each 3-C RMS field to remove noise attributed to low particle seeding densities, which were typically located in the bottom left and right corners. The mask is generated as a binarized image of the RMS field where axial velocity is less than 1 m/s. Therefore, instances such as the $X_{H_2} = 0\%$ and $X_{H_2} = 20\%$ conditions where it appears a bubble forms downstream are non-physical, as they are a result of post-processing. The mean progress variable $\bar{c} = 0.1$ contour in red also depicts the flame as being asymmetrical. This phenomenon has also been observed for other low-swirl burner geometries [44,45] and could be due to imperfections in manufacturing the swirl injector. It should be noted that flame asymmetry does not affect analysis of the turbulent flame speed.

Appendix D. Flamelet motion tracking

From post-processing, a considerable number of frames have been found where the flamefront either exhibits "jumping" or turbulence-induced turning (see dynamics in Fig. 12). As depicted in Figs. 21–22, such flamelet motion cannot be adequately captured by the algorithm. As a result, it becomes insufficient to track the entirety of the flame-front's motion if numerical artifacts persist between successive flame fronts. Therefore, this approach has been modified to evaluate only the leading point of the flame towards resolving the flamelet velocity S_{flame} component of the local flame displacement velocity S_f.

References

[1] Liu Z, Deng Z, Davis SJ, Giron C, Ciais P. Monitoring global carbon emissions in 2021. Nat Rev Earth Environ 2022;3:217–9.

[2] Ediger VS. An integrated review and analysis of multi-energy transition from fossil fuels to renewables. Energy Procedia 2019;156:2–6.

[3] Hermesmann M, Müller TE. Green, turquoise, blue, or grey? Environmentally friendly hydrogen production in transforming energy systems. Prog Energy Combust Sci 2022;90:100996.

[4] Trowell K, Goroshin S, Frost D, Bergthorson J. Aluminum and its role as a recyclable, sustainable carrier of renewable energy. Appl Energy 2020;275:115112.

[5] Bergthorson JM, Yavor Y, Palecka J, Georges W, Soo M, Vickery J, et al. Metal-water combustion for clean propulsion and power generation. Appl Energy 2017;186(1):13–27.

[6] Hydrogen strategy for Canada: Seizing the opportunities for hydrogen, a call to action. Tech. rep., Canada; 2020.

[7] The future of hydrogen: Seizing today's opportunities. Tech. rep., IEA; 2019.

[8] Hawkes ER, Chen JH. Direct numerical simulation of hydrogen-enriched lean premixed methane–air flames. Combust Flame 2004;138(3):242–58.

[9] Lim Z, Li J, Morgans AS. The effect of hydrogen enrichment on the forced response of CH$_4$/H$_2$/air laminar flames. Int J Hydrog Energy 2021;46(46):23943–53.

[10] Funke HHW, Beckmann N, Keinz J, Horikawa A. 30 Years of dry-low-Nox micromix combustor research for hydrogen-rich fuels—An overview of past and present activities. J Eng Gas Turbines Power 2021;143(7):071002.

[11] Durocher A, Fan L, Francolini B, Füri M, Bourque G, Sirois J, et al. Character-ization of a novel additive manufacturing micromix nozzle burning methane to hydrogen. J Eng Gas Turbines Power 2024;146(5):051009.

[12] Duan X, Li Y, Liu Y, Zhang S, Guan J, Lai MC, et al. Dilution gas and hydrogen enrichment on the laminar flame speed and flame structure of the methane/air mixture. Fuel 2020;281:118794.

[13] Schefer R, Wicksall D, Agrawal A. Combustion of hydrogen-enriched methane in a lean premixed swirl-stabilized burner. Proc Combust Inst 2002;29:843–51.

[14] Zhang W, Wang J, Lin W, Mao R, Xia H, Zhang M, et al. Effect of differential diffusion on turbulent lean premixed hydrogen enriched flames through structure analysis. Int J Hydrog Energy 2020;45:10920–31.

[15] Abbasi-Atibeh E, Bergthorson J. Differential diffusion effects in counter-flow premixed hydrogen-enriched methane and propane flames. Proc Combust Inst 2019;37:2399–406.

[16] Abbasi-Atibeh E, Bergthorson JM. The effects of differential diffusion in counter-flow premixed flames with dilution and hydrogen enrichment. Combust Flame 2019;209:337–52.

[17] An Q, Kheirkhah S, Bergthorson J, Yun S, Hwang J, June Lee W, et al. Flame stabilization mechanisms and shape transitions in a 3D printed, hydrogen enriched, methane/air low-swirl burner. Int J Hydrog Energy 2021;46:14764–79.

[18] Salusbury D. S. Experiments in laminar and turbulent premixed counter-flow flames at variable lewis number [Ph.D. thesis]. McGill University; 2014.

[19] Kuznetsov V, Sabel'nikov V, Libby P. Turbulence and combustion. Moscow, Russia: Hemisphere Publishing; 1986.

[20] Venkateswaran P, Marshall A, Hyuk Shin D, Noble D, Seitzman J, Lieuwen T. Measurements and analysis of turbulent consumption speeds of H$_2$/CO mixtures. Combust Flame 2011;158:1602–14.

[21] Driscoll JF. Turbulent premixed combustion: Flamelet structure and its effect on turbulent burning velocities. Prog Energy Combust Sci 2008;34:91–134.

[22] Shepherd I, Cheng RK. The burning rate of premixed flames in moderate and intense turbulence. Combust Flame 2001;127(3):2066–75.

[23] Berger L, Attili A, Pitsch H. Synergistic interactions of thermodiffu-sive instabilities and turbulence in lean hydrogen flames. Combust Flame 2022;244:112254.

[24] Bray KNC, Cant RS. Some applications of Kolmogorov turbulence research in the field of combustion. Proc R Soc A 1991;434(1890):217–40.

[25] Filatyev SA, Driscoll JF, Carter CD, Donbar JM. Measured properties of turbulent premixed flames for model assessment, including burning velocities, stretch rates, and surface densities. Combust Flame 2005;1–21.

[26] Bradley D. How fast can we burn? Symp (Int) Combust 1992;24(1):247–62.

[27] Anand M, Pope S. Calculations of premixed turbulent flames by PDF methods. Combust Flame 1987;67(2):127–42.

[28] Syreed N, Béer JM. Combustion in swirling flows: A review. Combust Flame 1974;23(2):143–201. http://dx.doi.org/10.1016/0010-2180(74)90057-1.

[29] Cheng R, Littlejohn D, Strakey P, Sidwell T. Laboratory investigations of a low-swirl injector with H$_2$ and CH$_4$ at gas turbine conditions. Proc Combust Inst 2009;32:3001–9.

[30] Law CK. Combustion physics. New York: Cambridge University Press; 2006.

[31] Abbasi-Atibeh E. The effects of differential diffusion in counter-flow premixed flames with dilution and hydrogen enrichment [Ph.D. thesis], McGill University; 2019.

[32] Bouvet N, Halter F, Chauveau C, Yoon Y. On the effective Lewis number formulations for lean hydrogen/hydrocarbon/air mixtures. Int J Hydrog Energy 2013;38(14):5949–60.

[33] University of California at San Diego. Chemical-kinetic mechanisms for com-bustion applications. 2016, San Diego Mechanism web page, Mechanical and Aerospace Engineering (Combustion Research).

[34] Chen X, Wang Y, Zirwes T, Zhang F, Bockhorn H, Chen Z. Heat re-lease rate markers for highly stretched premixed CH$_4$/air and CH$_4$/H$_2$/air flames. Energy Fuels 2021;35(16):13349—-13359. http://dx.doi.org/10.1021/acs.energyfuels.1c02187.

[35] Clemens N. Flow imaging. In: Encyclopedia of science and technology. New York: Wiley-Interscience; 2002.

[36] Knowledge United. Stereo PIV. 2008.

[37] Bell J, Daya MS, Shepherd IG, Johnson MR, Cheng RK, Grcar JF, et al. Numerical simulation of a laboratory-scale turbulent V-flame. Proc Natl Acad Sci 2005;102(29):10006–11.

[38] Pavlidis T. Algorithms for graphics and image processing. Springer Science & Business Media; 2012.

[39] Chakraborty N, Hartung G, Katragadda M, Kaminski C. Comparison of 2D and 3D density-weighted displacement speed statistics and implications for laser based measurements of flame displacement speed using direct numerical simulation data. Combust Flame 2011;158(7):1372–90.

[40] Cheng RK. Low-swirl combustion. In: The gas turbine handbook. 2006, p. 241–55.

[41] Dinkelacker F, Manickam B, Muppala SPR. Modelling and simulation of lean pre-mixed turbulent methane/hydrogen/air flames with an effective Lewis number approach. Combust Flame 2011;1742–9.

[42] Marshall A, Lundrigan J, Venkateswaran P, Seitzman J, Lieuwen T. Fuel effects on leading point curvature statistics of high hydrogen content fuels. Proc Combust Inst 2015;35:1417–24.

[43] Boateng A. Rotary kilns: Transport phenomena and transport processes. Elsevier; 2016.

[44] Day M, Tachibana S, Bell J, Lijewski M, Beckner V, Cheng RK. A combined computational and experimental characterization of lean premixed turbulent low swirl laboratory flames II. Hydrogen flames. Combust Flame 2015;162:2148–65.

[45] Therkelsen PL, Littlejohn D, Cheng RK. Parametric study of low-swirl injector geometry on its operability. In: Proceedings of ASME turbo expo 2012, vol. 44687. 2012, p. 309–18.